

Do high redshift QSOs and GRBs corroborate JWST?

Eoin Ó Colgáin,¹ M. M. Sheikh-Jabbari,² and Lu Yin³

¹*Atlantic Technological University, Ash Lane, Sligo F91 YW50, Ireland*

²*School of Physics, Institute for Research in Fundamental Sciences (IPM), P.O.Box 19395-5531, Tehran, Iran*

³*Asia Pacific Center for Theoretical Physics, Postech, Pohang 37673, Korea*

The James Webb Space Telescope (JWST) is reporting unexpectedly massive high redshift galaxies that appear challenging from the Λ CDM perspective. Interpreted as a problem of cosmological origin, this necessitates Planck underestimating either matter density Ω_m or physical matter density $\Omega_m h^2$ at higher redshifts. Through standard frequentist profile likelihoods, we identify corroborating quasar (QSO) and gamma-ray burst (GRB) data sets where Ω_m increases with effective redshift z_{eff} , with Ω_m remaining anomalously large at higher redshifts. While the variation of Ω_m with z_{eff} is at odds with the Λ CDM model, demarcating frequentist confidence intervals through differences in χ^2 in profile likelihoods, the prevailing technique in the literature, points to 3.9σ and 7.9σ tensions between GRBs and QSOs, respectively, and Planck- Λ CDM. We explain the approximations inherent in the existing profile likelihood literature, and highlight fresh methodology that generalises the prescription. We show that alternative methods, including Bayesian approaches, lead to similar tensions.

I. INTRODUCTION

Preliminary James Webb Space Telescope (JWST) data has revealed a bevy of high-redshift galaxies with intriguingly large stellar masses [1–8]. This unforeseen finding has seeded investigations into observational systematics [9–15] and speculations on new astrophysics. The latter musings range from more mundane changes to the star formation rate [16–22] to exotic physics that could explain the origin of the galaxies, such as accelerated growth through massive seed black holes [23, 24] and primordial black holes [25–27]; invoking primordial magnetic fields [28]; primordial density fluctuations [29]; cosmic string loops [30–32]; changes to the dark matter (DM) paradigm [33–40]. While DM represents a cornerstone in the Lambda-Cold Dark Matter (Λ CDM) cosmological model, one could also consider relaxing other Λ CDM assumptions, notably dark energy described by the cosmological constant Λ [41–46], in order to alleviate any tension. More generally, one may radically rethink cosmology to allow more time for galaxies to form [47–49]. In the big picture, it is imperative to tease apart the astrophysical and cosmological implications of JWST observations, otherwise JWST can *never* challenge Λ CDM. Tellingly, a host of studies inspired by JWST reaffirm that Λ CDM is fine [50–53].

Separately, Λ CDM is troubled by persistent, independent anomalies, most notably H_0 and S_8 tensions (reviewed in [54–56]). Admittedly, Λ CDM is a big beast, and JWST anomalies *on their own* may not have enough firepower to bring an end to the normal (Λ CDM) science cycle. For this reason, it is instructive to establish that independent anomalies are indeed consistently pointing to qualitatively similar deviations from Planck- Λ CDM [57] behaviour. To that end, it is noteworthy that popular resolutions to H_0 tension, which introduce pre-recombination physics to adjust the BAO scale [58–64], typically lead to larger values of physical matter density $\Omega_m h^2$ relative to Planck [57], thereby alleviating tension with JWST [13, 65–68]. See also [68, 69] for implications of JWST data for other models claiming to alleviate H_0 tension.

In this letter, we showcase a synergy between an existing Λ CDM anomaly and JWST observations. Concretely, it has

been proposed that quasars (QSOs) are standardisable through a non-linear UV, X-ray flux relation popularised by Risaliti & Lusso [70]. This begets an anomaly, whereby the resulting QSO data set [71, 72] favours smaller luminosity distances than Planck- Λ CDM [57], especially at higher redshifts, $z \gtrsim 1.5$ [71, 72]. Translated into the flat Λ CDM cosmology, this implies a larger value of matter density Ω_m relative to Planck [73]. As can be seen from Fig. 1 of [68], not only does JWST data prefer larger values of physical matter density $\Omega_m h^2$, as claimed in [13, 65–68],¹ JWST also prefers larger values of matter density today Ω_m . The point of this letter is that the larger values of Ω_m and $\Omega_m h^2$ preferred by the Risaliti-Lusso QSOs are also preferred by JWST, at least at the level of qualitative comparison. Since the standardisability of the Risaliti-Lusso QSOs has been openly challenged [74–80], we identify a gamma-ray burst (GRB) data set, which apparently passes standardisable candle tests failed by QSOs [81], that exhibits the same trend. Along the way, we explain the limitations of prevailing methods for determining frequentist confidence intervals from profile likelihoods and comment on fresh methodology [82] (see also [83, 84]) that generalises existing methods.

II. JWST ANOMALY

We begin by reviewing JWST observations of massive high redshift galaxies that appear anomalous from the Λ CDM perspective [1–8]. The point of this section is to serve as an appetiser for later QSO and GRB anomalies that appear to be pointing to consistent deviations from the Planck- Λ CDM cosmology [57]. Concretely, we will demonstrate that larger Ω_m and $\Omega_m h^2$ values relative to the Planck- Λ CDM help alleviate tensions with JWST. Our findings in this section are expected since a host of papers claim that tension between Planck- Λ CDM and JWST can be reduced by increasing ei-

¹Note that $h := H_0/100$ is simply a multiplicative factor of the Hubble constant H_0 .

ther matter density today Ω_m [68] or physical matter density $\Omega_m h^2$ [65–68].

We quickly review how one arrives at these conclusions. Basically, one needs to compute the comoving number or mass density of haloes. To begin, the dark matter (DM) halo mass function $dn(M, z)/dM$ quantifies the number of DM haloes of mass M per unit mass per unit co-moving volume at redshift z :

$$\frac{dn}{dM} = -\frac{\rho_m^{(0)}}{M} \frac{d \ln \sigma}{dM} f(\sigma), \quad (1)$$

where $\rho_m^{(0)}$ is the matter energy density today, $\sigma(R, z)$ is the variance of matter density fluctuations in a sphere of comoving radius R at redshift z , and $f(\sigma)$ is defined through the Sheth-Tormen prescription for DM haloes [85]:

$$f(\sigma) = A \sqrt{\frac{2a}{\pi}} \left[1 + \left(\frac{\sigma^2}{a\delta_c^2} \right)^p \right] \frac{\delta_c}{\sigma} \exp\left(-\frac{\delta_c^2 a}{2\sigma^2}\right). \quad (2)$$

Here we follow [45] and adopt the numbers $A = 0.322$, $a = 0.707$, $p = 0.3$ and $\delta_c = 1.686$. As is the norm, the mass M within a sphere of comoving radius R is simply the volume of the sphere times matter density today, $M = \frac{4}{3}\pi R^3 \rho_m^{(0)}$, and the variance $\sigma(R, z)$ takes the form,

$$\sigma^2(R, z) = \frac{1}{2\pi^2} \int_0^\infty dk k^2 P(k, z) W^2(kR), \quad (3)$$

where $P(k, z)$ is the power spectrum of matter density fluctuations and $W(x) = 3(\sin x - x \cos x)/x^3$.

At this point, one has all the ingredients to calculate the cumulative comoving mass density of stars contained in galaxies more massive than M_\star [65]:

$$\rho(> M_\star, z) = \epsilon f_b \int_{M_{\text{halo}}}^\infty dM M \frac{dn(M, z)}{dM}, \quad (4)$$

where $f_b := \Omega_b/\Omega_m$ is the cosmic baryon fraction and ϵ is the efficiency of converting gas into stars. We assume f_b and ϵ to be cosmology-independent constants and fix them to $f_b = 0.156$ and $\epsilon = 0.32$. One is now in a position to produce Fig. 1 and Fig. 2. What they demonstrate simply backs up observations made elsewhere in the literature, namely that increasing both matter density Ω_m and physical matter density $\Omega_m h^2$ relative to the Planck values alleviates tension with observations [65–68].

Note that Ω_m and h are constant fitting parameters, alternatively cosmological parameters, in the Λ CDM model, which cannot vary without running into an inconsistency between the Λ CDM model and observations. While this subtlety is typically glossed over in Bayesian analysis, from the perspective of physics² it is important to check that the Λ CDM cosmological parameters are not redshift dependent [86].

²It is difficult to call cosmology a sub-branch of physics unless one conducts the consistency tests that physicists routinely perform elsewhere.

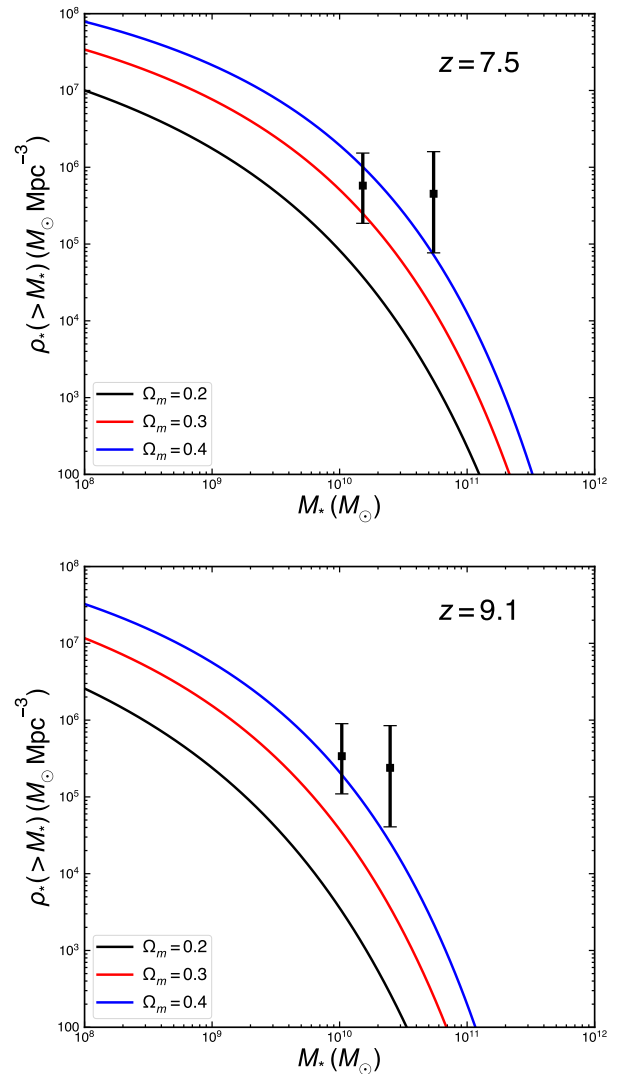


FIG. 1. The comoving stellar mass density contained within galaxies more massive than M_\star at $z \approx 7.5$ (above) and $z \approx 9.1$ (below). With fixed cosmic baryon fraction, f_b , and fixed efficiency of converting gas into stars, ϵ , increasing Ω_m alleviates tensions with the Llabé et al. [2] data points.

It should be stressed that the purpose of this section is to make the paper as self-contained as possible. Evidently, there appears to be some tension between the Planck- Λ CDM model and JWST. Of course, this tension may be overcome through new astrophysics. For example, it is evident that increasing the efficiency ϵ can also alleviate the problem. What we will now show is that high redshift cosmological probes have a preference for the larger Ω_m values that would help alleviate JWST anomalies. This may be a coincidence, and neither QSOs nor GRBs may make sense as cosmological probes, but given the synergy, further study is warranted. We expect that Type Ia supernovae (SNe) samples will be able to confirm or refute these observations in QSOs/GRBs once we have higher redshift samples.

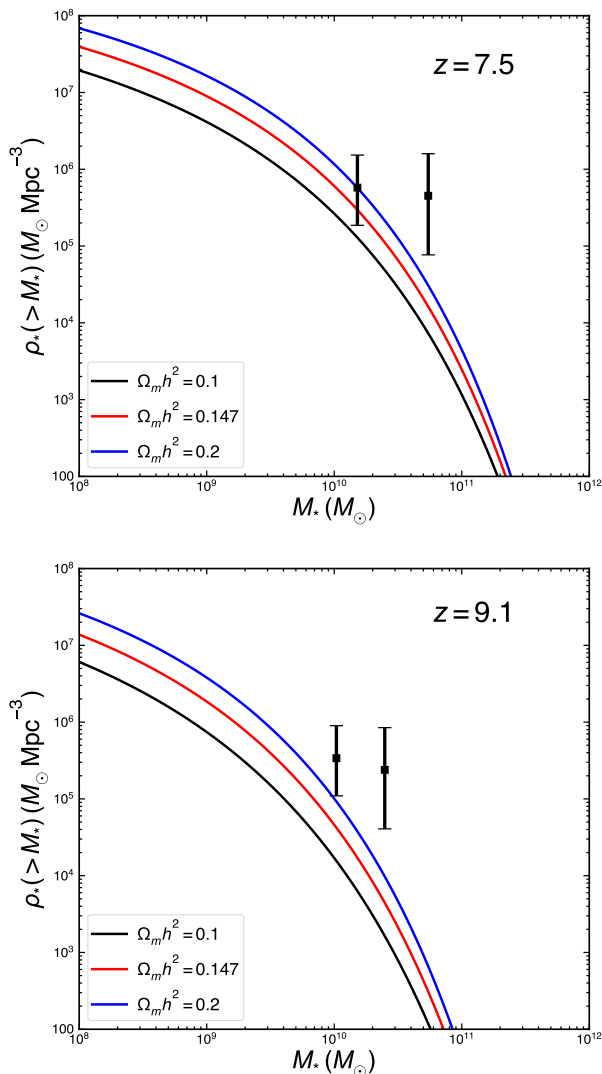


FIG. 2. The comoving stellar mass density contained within galaxies more massive than M_* at $z \approx 7.5$ (above) and $z \approx 9.1$ (below). With fixed cosmic baryon fraction, f_b , and fixed efficiency of converting gas into stars, ϵ , increasing $\Omega_m h^2$ alleviates tensions with the Labbé et al. [2] data points.

III. FREQUENTIST CONFIDENCE INTERVALS

In the literature frequentist confidence intervals typically approximate likelihoods as Gaussian distributions. A case in point is the Fisher matrix. As is evident from section 2.6 of [87], one can Taylor expand the likelihood $\mathcal{L}(\theta)$ about the maximum likelihood estimator (MLE) $\bar{\theta}$ dropping terms beyond quadratic order. This truncation of the expansion evidently throws information away, and as a result, one is *approximating* the likelihood about its peak as a Gaussian.³ The

³Note, for equation (33) of [87] to make sense as a 68% confidence interval, one must be implicitly integrating the likelihood, suitably normalised, over the parameter θ .

second frequentist method highlighted in [87] is profile likelihoods. Concretely, one constructs the profile likelihood ratio,

$$R(\theta) = \frac{\mathcal{L}(\theta, \hat{\psi})}{\mathcal{L}(\hat{\theta}, \hat{\psi})}, \quad (5)$$

where θ is the parameter of interest, ψ denotes auxiliary parameters, $\hat{\psi}$ is the value of ψ that maximises the likelihood $\mathcal{L}(\theta, \psi)$ for fixed θ , and $(\hat{\theta}, \hat{\psi})$ denote the values of (θ, ψ) that globally maximise the likelihood $\mathcal{L}(\theta, \psi)$. We note that the denominator is a constant so that the numerator $\mathcal{L}(\theta, \hat{\psi})$, called a profile likelihood, and the profile likelihood ratio are identical up to a constant. For this reason, we will use the terminology profile likelihood and profile likelihood ratio interchangeably; we hope the meaning is clear from the context.

In our work, we will study profile likelihoods with one degree of freedom, $\theta = \Omega_m$. The logic then goes that one invokes Wilks' theorem [88], which states for large enough samples profile likelihoods are close to Gaussian:

$$\mathcal{L}(\theta, \hat{\psi}) \propto e^{-\frac{c}{2}(\theta - \bar{\theta})^2} (1 + O(1/\sqrt{n})), \quad (6)$$

where c is a positive constant, $\bar{\theta}$ is the MLE for the parameter θ , n is the size of the sample, and we have specialised to the case of interest with one degree of freedom θ . Equation (6) is essentially equation (7) from [88]. It should be evident that Wilks' theorem makes assumptions so that the profile likelihood converges to a Gaussian distribution in the large sample limit $n \rightarrow \infty$. As a result, $-2 \ln R(\theta)$ converges to a chi-squared distribution in the same limit.

Making use of Wilks' theorem [88], the prescription is that 100 $\alpha\%$ confidence intervals correspond to the values of $\Delta\chi^2$ satisfying the equation [87]:

$$\alpha = \int_{y=0}^{y=\Delta\chi^2} \frac{1}{\sqrt{2\pi y}} e^{-\frac{1}{2}y} dy, \quad (7)$$

where we have specialised to the chi-squared distribution with one degree of freedom and employed $\Gamma(\frac{1}{2}) = \sqrt{\pi}$. Integrating the right hand side to $\Delta\chi^2 = 1$ and $\Delta\chi^2 = 3.9$ one finds $\alpha = 0.6827$ and $\alpha = 0.9517$, corresponding to 68% and 95% confidence intervals, respectively. A key point here is that if X is a random variable with a standard normal distribution with probability density function (PDF),

$$f_X(x) = \frac{1}{\sqrt{2\pi}} e^{-\frac{1}{2}x^2}, \quad \int_{-\infty}^{+\infty} f_X(x) dx = 1, \quad (8)$$

then it is easy to prove that $Y = X^2$ has the chi-squared distribution PDF⁴

$$f_Y(y) = \frac{1}{\sqrt{2\pi y}} e^{-\frac{1}{2}y}, \quad \int_{-\infty}^{+\infty} f_Y(y) dy = 1. \quad (9)$$

⁴en.wikipedia.org/wiki/Proofs_related_to_chi-squared_distribution

Thus, one has the result

$$\alpha = \int_0^{\Delta\chi^2} \frac{1}{\sqrt{2\pi y}} e^{-\frac{1}{2}y} dy = \int_{-\sqrt{\Delta\chi^2}}^{+\sqrt{\Delta\chi^2}} \frac{1}{\sqrt{2\pi}} e^{-\frac{1}{2}x^2}. \quad (10)$$

In other words, integrating the chi-squared distribution with one degree of freedom between $\Delta\chi^2 = 0$ and $\Delta\chi^2 = 1$ is equivalent to integrating a standard normal distribution between $-\sqrt{\Delta\chi^2}$ and $+\sqrt{\Delta\chi^2}$. Specialising to the region of parameter space with $\Delta\chi^2 \leq 1$, we recognise from equation (10) that the 68% confidence intervals one recovers are precisely the 1σ confidence interval of a Gaussian. So, in summary, equation (7) *approximates* confidence intervals and this approximation becomes *exact* in the $n = \infty$ limit whereby the profile likelihood (10) is Gaussian.

As an aside, there is one further subtlety worth discussing with the $\Delta\chi^2 \leq 1$ and $\Delta\chi^2 \leq 3.9$ prescription for 68% and 95% confidence intervals. Wherever the confidence intervals are impacted by a boundary, one should make use of the Feldman-Cousins prescription [89]. We remark that the prescription is employed in [83], but since the profile likelihood is Gaussian to a good approximation, and the $\Delta\chi^2 \leq 1$ interval is not impacted by the boundary, the methodology is redundant for 68% confidence intervals. More concretely, from Fig. 2 of [83] it is evident that the boundary starts to impact results at 95% confidence interval corresponding to $\Delta\chi^2 \leq 3.9$. In [90] the Feldman-Cousins prescription is employed to greater effect, but we observe that the authors assume that their profile likelihoods follow equations (4.2) and (4.3) from the Feldman-Cousins paper [89], i. e. Gaussian profile likelihoods are assumed.⁵

We have hopefully convinced the reader that frequentist confidence intervals in cosmology rest heavily on Gaussian distributions.⁶ This begs the question, how does one treat generic profile likelihoods? To that end [82] (see also [83, 84]) suggests the following prescription. To extract the 68% confidence interval for the profile likelihood, one normalises the profile likelihood ratio by the total area under the curve,

$$w(\theta) = \frac{R(\theta)}{\int R(\theta) d\theta}, \quad (11)$$

and solves the equation

$$\int_{\theta^{(1)}}^{\theta^{(2)}} w(\theta) d\theta = 0.68, \quad w(\theta^{(1)}) = w(\theta^{(2)}). \quad (12)$$

⁵We thank Giacomo Galloni for correspondence on this point.

⁶It is often argued in the literature that one can reparameterise to get a Gaussian profile likelihood, e. g. [91]. This is true, but one needs to make sure that reparameterisations are physical. For example, the degeneracies or banana-shaped contours in MCMC posteriors in the (H_0, Ω_m) -plane in [84] can be removed by redefining (H_0, Ω_m) as $(H_0, \Omega_m h^2)$. Since $\Omega_m h^2$ is well constrained, this should lead to a Gaussian profile in $\Omega_m h^2$. The question is, what does one do about H_0 , a universal constant in all FLRW models? How does one reparameterise H_0 ? It is also worth noting that H_0 may be directly and definitively measured by local distance ladder measurements in a cosmological model-independent way assuming homogeneity and isotropy at cosmological scales.

To get 95% (2σ) and 99.7% (3σ) confidence intervals one simply changes the number on the right hand side of equation (12). It should be noted that equations (7) and (8) are more or less equations (2) and (3) from [83]. The content of equation (12) is that one builds 68% confidence intervals outwards from the peak of the profile likelihood ratio, $R(\hat{\theta}) = 1$, by steadily including points in the θ parameter space that are steadily less likely until one reaches 68% of the area under the profile likelihood curve. It should be clear from (6) and (10) that for a Gaussian profile likelihood we can expect the 68% confidence interval to agree with the $\Delta\chi^2 \leq 1$ confidence interval one gets by exploiting Wilks' theorem. Nevertheless, it should be stressed that Wilks' theorem is at best an approximation. As a further comment, one may worry that integrating the likelihood, suitably normalised, over the parameter is difficult to justify. However, here one can invoke Bayes' theorem, where assuming uninformative uniform priors, as we do here, the posterior probability of the parameter θ given the data d , $P(\theta|d)$, must reduce to the likelihood $\mathcal{L}(\theta)$ up to a normalising constant, $P(\theta|d) \propto \mathcal{L}(\theta)$ (see equation (74) of [87]).

IV. QSO ANOMALY

We begin by studying changes in the best fit Λ CDM parameters (H_0, Ω_m) in QSO data [70–72]. Trends of increasing Ω_m with effective redshift have been reported [92–95] across a number of observables, including Type Ia SNe, and here we revisit findings with fresh methodology. Previously, the observation that Ω_m increased with effective redshift rested upon i) extremising the log-likelihood to identify best fits and ii) Markov Chain Monte Carlo (MCMC) posteriors [92]. Both analyses imposed an admittedly physical but restrictive prior on matter density, $0 \leq \Omega_m \leq 1$.

Here we relax this prior to allow $\Omega_m > 1$ values while exploiting frequentist analysis introduced in section III. Relaxing the prior $\Omega_m \leq 1$ allows the QSO data to constrain the Λ CDM model without preconceptions. Moreover, while one typically constructs profile likelihoods by isolating a fitting parameter of interest and extremising the log-likelihood with respect to the remaining parameters, here we will also employ methodology that recycles and bins the MCMC chain [82, 84].⁷ We remark that one traditionally maximises the log-likelihood, but it allows a more direct comparison between Bayesian and frequentist methods if one starts from information in the same MCMC chain. As we shall see, whether one maximises the log-likelihood or bins the MCMC chain, the difference is negligible and it can be improved by running longer MCMC chains, e. g. [84].

Recall the Risaliti-Lusso procedure for standardising QSOs [70]. At its heart, one assumes a UV, X-ray luminosity relation that is intrinsic to QSOs:

$$\log L_X = \beta + \gamma \log L_{UV}, \quad (13)$$

⁷See [87] for a discussion on binning the MCMC chain to construct profile likelihoods.

where β and γ are constant fitting parameters. Through the standard luminosity-flux relation, $L = 4\pi D_L(z)^2 F$ with luminosity distance $D_L(z)$, (13) is equivalent to the UV, X-ray flux relation:

$$\log F_X = \tilde{\beta} + \gamma \log F_{UV} + 2(\gamma - 1) \log D_L(z), \quad (14)$$

where $\tilde{\beta} = \beta + (\gamma - 1) \log 4\pi$. Equation (13) is empirically motivated, but a physical backstory has been provided in terms of an interaction between the accretion disc of the Active Galactic Nucleus (AGN) and the X-ray Corona. This would allow photons to inverse Compton scatter from UV to X-ray without hot electrons losing their energy. The precise physical mechanism is unclear, but models exist to explain the physics [96–98]. Returning to the empirical result, the key point is that given observations of the X-ray flux F_X and UV flux F_{UV} , one can constrain the cosmological model Hubble parameter $H(z)$ through the luminosity distance

$$D_L(z) = c(1+z) \int_0^z \frac{1}{H(z')} dz'. \quad (15)$$

Throughout, we will assume the (flat) Λ CDM model with

$$H(z) = H_0 \sqrt{1 - \Omega_m + \Omega_m(1+z)^3}. \quad (16)$$

The parameters (H_0, Ω_m) arise as integration constants in either the Friedmann equation or the matter continuity equation.⁸ Alternatively put, *mathematically* neither parameter can change with effective redshift, however it remains to be seen if this is the case *observationally*. These consistency checks have been overlooked in cosmology, but they are well motivated [86]. We will see that, as highlighted initially in [71, 73, 99], there is a strong tension between the QSO data and the Λ CDM model. However, in contrast to earlier work, the inconsistency need not be relative to a specific value of Ω_m preferred by a different data set, e. g. Planck CMB data [57], but may be regarded as inconsistency driven by the non-constancy of integration constants. The contradiction between data and model is difficult to ignore.

Evidently, (13) is a working assumption. It is the subject of a growing body of work in the cosmology literature either questioning [74–80] or refining the Risaliti-Lusso prescription [100, 101].⁹ In particular, it has been argued in [80] that the Risaliti-Lusso QSOs are impacted by extinction, but this effect may not be large enough to explain the discrepancy seen in the Hubble diagram [102]. Here, it is worth stressing that QSOs represent emerging cosmological probes [103] and considerable work remains to turn the proposal into standardisable candles on par with Type Ia SNe, where developments span 3 decades. See [104] for a historical account of the quest to construct a QSO Hubble diagram. Nevertheless, in defence

of the Risaliti-Lusso methodology, it should be noted that the logarithms of X-ray and UV fluxes show an apparent correlation (see for example Figs. 3 and 4 of [70]), and to first approximation it is valid to fit a line to any empirical relation.¹⁰ Ultimately, our goal here is not to question (13), but to maintain an open mind and treat it as a working assumption in order to study the implications. The point of the work is to draw a parallel between the preference of Risaliti-Lusso QSOs¹¹ and JWST observations for larger Ω_m and larger $\Omega_m h^2$ values at higher redshifts. Along the way, we will comment on the tension between the QSO data set and the Planck- Λ CDM model using the frequentist methods in section III.

The QSO data set we employ consists of 2421 QSOs spanning the redshift range $0.009 \leq z \leq 7.5413$ [72]. The data set comprises the redshifts z_i , X-ray and UV fluxes ($F_{X,i}, F_{UV,i}$) and their corresponding errors ($\sigma_{F_{X,i}}, \sigma_{F_{UV,i}}$). There is considerable scatter in the QSO data and this is absorbed through an intrinsic error or intrinsic dispersion parameter δ [70]. Thus, restricting our attention to the Λ CDM model (16), there are three nuisance parameters (β, γ, δ) in addition to the cosmological parameters (H_0, Ω_m). As is the case with Type Ia SNe data sets, where the absolute magnitude M_B is degenerate with H_0 , here β and H_0 are degenerate. To overcome this degeneracy, one typically assumes a canonical value of $H_0 = 70$ km/s/Mpc and fits ($\Omega_m, \beta, \gamma, \delta$) to the data. To do so, we consider the log-likelihood [70–72],

$$\begin{aligned} \ln \mathcal{L} &= -\frac{1}{2} \left[\chi^2 + \sum_{i=1}^N \ln(2\pi s_i^2) \right], \\ &= -\frac{1}{2} \sum_{i=1}^N \left[\frac{(\log F_{X,i}^{\text{obs}} - \log F_{X,i}^{\text{model}})^2}{s_i^2} + \ln(2\pi s_i^2) \right] \end{aligned} \quad (17)$$

where $\log F_{X,i}^{\text{model}}$ is defined in (14). Here, $s_i^2 = \sigma_{\log F_{X,i}^{\text{obs}}}^2 + \delta^2$ in (17) contains the measurement error on the observed flux $\log F_{X,i}^{\text{obs}}$ and the intrinsic dispersion. Following the Risaliti-Lusso prescription, the F_{UV} errors can be safely ignored [70] on the grounds that both F_X and F_{UV} errors are considerably smaller than δ .

A. Ω_m trend

In Table I we record frequentist 68% confidence intervals for Ω_m as the redshift range of the sample is increased. The corresponding profile likelihood ratios are shown in Fig. 3, where the cyan curve corresponds to the full sample. As explained above, we fix H_0 to a canonical value, scan over Ω_m

⁸ H_0 is an integration constant in the Friedmann equations and $\rho_m(z=0) \propto H_0^2 \Omega_m$ is an integration constant in the matter continuity equations. As a result, Ω_m must be constant.

⁹Despite the corrections imposed on the QSO data, a residual increasing trend of the Ω_m parameter is still reported [101].

¹⁰Unsurprisingly, the slope γ is robust to changes in redshift [105–109]. However, it is imperative from (14) that the y-intercept is not a constant in the $\log F_X - \log F_{UV}$ plane and that it decreases (note $\gamma \approx 0.6 < 1$) with increasing redshift/luminosity distance for any cosmology. Such a trend is visible in Fig. 4 of [70], but a greater number of redshift bins is warranted.

¹¹Similar trends are also seen in Type Ia SNe and observational Hubble data [93–95], but high redshift subsamples are smaller than QSO subsamples.

values in the range $\Omega_m \in [0, 3]$, and for each value of Ω_m we identify the maximum value of the likelihood at each value of Ω_m , $\mathcal{L}_{\max}(\Omega_m)$. Note, our choice of Ω_m bound allows us to track movements in the profile likelihood peak and confirm that the profile likelihood is well constrained, i. e. falls off at smaller and larger values of Ω_m . That being said, it is evident that the bounds are not generous enough to accommodate the profile likelihood for the full sample (cyan curve).

Note, it is observed in [75] that the variations in cosmological parameters across different models become more severe at higher redshifts when one fits QSO data. This was interpreted as evidence for the non-standardisability of the Risaliti-Lusso QSOs. However, as explained in [110], the biggest jumps in cosmological parameters happen when the curvature parameter Ω_k is introduced, but this can be traced to the added flexibility that $\Omega_k < 0$ gives to lower the distance modulus or luminosity distance at higher redshifts. The key point here is that the full QSO data set prefers $\Omega_m > 1$ values, so if one constrains Ω_m to the usual range, $0 \leq \Omega_m \leq 1$, one can get a better fit to the data through a curvature parameter Ω_k . In short, the Ω_m bounds prevent the QSO data from finding the $\Omega_m > 1$ MLE values. This should come as no surprise as a pronounced fall off in the distance modulus relative to Planck- Λ CDM is glaringly obvious at higher redshifts in Fig. 2 of [71]. Evidently, great care is required with QSOs over extensive redshift ranges. Thus, the point of Fig. 3 is to focus on evolution in the QSO sample at more accessible and conservative lower redshifts $z \lesssim 1$, while demonstrating that the increasing Ω_m trend with effective redshift persists to the full sample. We remark that once the profile likelihood peak enters $\Omega_m > 1$ parameter space, one can interpret this as negative dark energy density in the Λ CDM model.

Redshift	# QSOs	Ω_m (68%)	Ω_m ($\Delta\chi^2 \leq 1$)
$0 < z \leq 0.7$	398	< 0.793 (0.261)	$0.261^{+0.461}_{-0.251}$
$0 < z \leq 0.8$	543	$0.421^{+0.542}_{-0.391}$	$0.421^{+0.402}_{-0.281}$
$0 < z \leq 0.9$	680	$0.532^{+0.532}_{-0.311}$	$0.532^{+0.451}_{-0.281}$
$0 < z \leq 1$	826	$0.863^{+0.642}_{-0.391}$	$0.863^{+0.572}_{-0.361}$
$0 < z \leq 7.5413$	2421	$2.424 < (3)$	$2.545 < (3)$

TABLE I. The number of QSOs in redshift bins with 68% frequentist confidence intervals for Ω_m determined using the two methods outlined in section III. Ω_m best fits and confidence intervals increase with effective redshift. In the absence of an upper or lower bound we present the profile likelihood peak (MLE) in brackets.

Scanning over Ω_m and maximising the log-likelihood (17) leads to an array of $(\Omega_m, \mathcal{L}_{\max}(\Omega_m))$ values. Inevitably, there will be a global maximum \mathcal{L}_{\max} in the range $\Omega_m \in [0, 3]$. This allows us to construct the profile likelihood ratio,

$$\begin{aligned}
 R(\Omega_m) &= \frac{\mathcal{L}_{\max}(\Omega_m)}{\mathcal{L}_{\max}} = \exp\left(-\frac{1}{2}\Delta\chi^2\right), \\
 &= \exp\left(-\frac{1}{2}(\chi^2_{\min}(\Omega_m) - \chi^2_{\min})\right), \quad (18)
 \end{aligned}$$

which by construction peaks at an Ω_m value where $R(\Omega_m) = 1$.

The profile likelihoods $R(\Omega_m)$ for different redshift ranges are presented in Fig. 3. The cyan distribution has evidently been curtailed by our bounds on Ω_m and the distribution peaks at a larger $\Omega_m > 3$ value. What the cyan curve demonstrates is that there is a strong tension between the full QSO sample and canonical Planck values of $\Omega_m \sim 0.3$. However, as is clear from the plot, and earlier results from [92], QSOs restricted to lower redshifts prefer Planck Ω_m values. Even if QSOs are non-standardisable, this is a surprising coincidence. To extract the Ω_m 68% confidence intervals for each curve, one normalises by the total area under the curve (11) and solves equation (12).

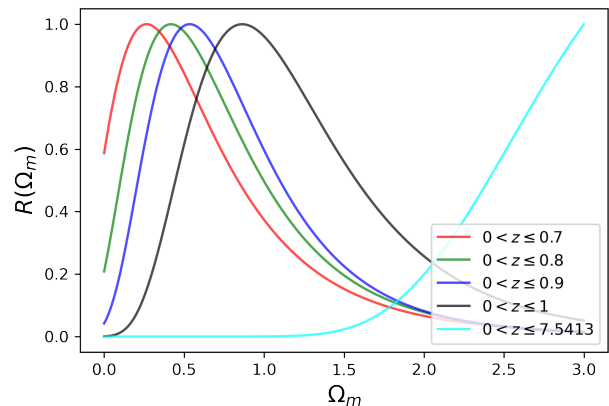


FIG. 3. Variation of profile likelihoods $R(\Omega_m)$ with increasing effective redshift of the QSO sample [72]. The Λ CDM parameter Ω_m is not a constant when confronted to the QSO data.

To be more concrete about our methodology, we break the $\Omega_m \in [0, 3]$ interval up into 300 intervals of $\Delta\Omega_m \approx 0.01$ and maximise the log-likelihood for the auxiliary parameters (β, γ, δ) at each discrete value of Ω_m . Throughout, we make sure that the values of (β, γ, δ) that maximise (17) are not impacted by our bounds on those parameters. Even without interpolating the discrete values, this led to the smooth curves in Fig. 3. To perform integration, we made use of Simpson's rule. The resulting confidence intervals are presented in the third column in Table I. It is worth noting that the profiles have long non-Gaussian tails in the direction of larger Ω_m values. This behaviour is expected when one confronts the Λ CDM model to binned luminosity distance data and removes the low redshift observables [92]. Note, we have not binned the data, but the Risaliti-Lusso QSO samples become sparse at low redshift, so the redshift distribution of the observables is the same.

One interesting feature of our analysis is that the $\Delta\chi^2 \leq 1 \Leftrightarrow R(\Omega_m) \geq 0.607$ prescription leads to smaller, less conservative 68% confidence intervals in column 4 in Table I. The 68% confidence intervals for the full sample need to be treated with caution as the peak of the profile likelihood exceeds our upper bound $\Omega_m = 3$. Nevertheless, it is a given that one can treat $\Omega_m = 3$ as a lower bound on the position of the peak. We can then get a *lower bound* on the tension with the 1σ Planck upper bound $\Omega_m \leq 0.322$ [57]. Translated into the profile

likelihood ratio, one has $R(\Omega_m) \leq 2.4 \times 10^{-14}$ corresponding to $\Delta\chi^2 \geq 62.7$ and a $\sim 7.9\sigma$ disagreement between the QSOs and Planck. Once again bearing in mind the obvious caveat that the peak of our profile likelihood is beyond $\Omega_m = 3$, one may employ (11) and (12). Doing so, one finds that the Planck value is disfavoured at 99.9999999999994% confidence level or $\sim 7.8\sigma$. It is interesting that both our methodologies agree. Given the close agreement, we can infer that cyan curve bears a close approximation to a Gaussian in the redshift range of interest. Let us emphasise again that this is a lower bound because as is clear from Fig. 3 the bulk of the profile likelihood distribution is beyond $\Omega_m = 3$. Relaxing that prior will mean that the tail of the profile likelihood corresponding to the Planck value will correspond to an even smaller percentage of the area under the curve. To find such a strong tension with standard frequentist methods is a little surprising. However, let us stress here that our profile likelihood is unobstructed as far as the Planck value, so there is no problem inferring the confidence level of lower bounds based on the $\Delta\chi^2$ prescription. The Feldman-Cousins prescription [89] is not necessary for lower confidence intervals.

Moving along, our profile likelihood analysis to this point has been relatively standard frequentist analysis. This provides a complementary perspective on earlier results based on best fits and MCMC posteriors [92]. Previously, it was evident that Ω_m increased from a Planck value $\Omega_m \approx 0.3$ to larger values, but our one-dimensional Ω_m MCMC posteriors were impacted by restrictive $\Omega_m \in [0, 1]$ priors [93]. Here, we have relaxed the priors, and it is evident that the 68% confidence intervals for QSOs in the redshift range $0 < z \leq 1$ have shifted to the extent that the canonical $\Omega_m \approx 0.3$ falls outside the confidence intervals, irrespective of the method used to identify confidence intervals. The analysis here provides confirmation that the Ω_m best fits and corresponding confidence intervals shift to larger Ω_m values as one increases the QSO redshift range. Noting that Ω_m is by definition a constant, since it is related to an integration constant, this underscores the tension between the QSO sample and the Λ CDM model. In short, the tension is evident throughout the sample.

Before moving to study $\Omega_m h^2$ in the next subsection, it is interesting to compare profile likelihoods from maximising the log-likelihood, i. e. optimisation or gradient descent, with the corresponding result from binning MCMC chains [82, 84]. While the latter allows a better comparison between Bayesian and frequentist methods, as one is exploiting the MCMC chain throughout, one worry is that MCMC may poorly identify $\mathcal{L}_{\max}(\Omega_m)$. Focusing on QSOs in the lowest redshift range, $0 < z \leq 0.7$, in Fig. 4 we present $R(\Omega_m)$ from a binned, converged MCMC chain in blue dots alongside the optimised $R(\Omega_m)$ in red. There is noticeable scatter in the blue dots and they visibly underestimate $\mathcal{L}_{\max}(\Omega_m)$ and $R(\Omega_m)$. This is the expected outcome because the goal is to maximise $\mathcal{L}_{\max}(\Omega_m)$, but any MCMC algorithm prioritises exploring parameter space over optimisation. That being said, any difference to the inferred 68% confidence interval is negligible. One can evidently improve the agreement by running a longer MCMC chain, e. g. as in [84].

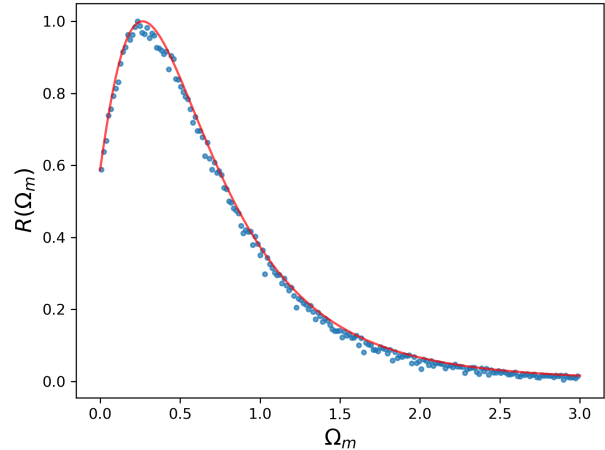


FIG. 4. $R(\Omega_m)$ from binned, converged MCMC chain in blue dots versus maximisation of the log-likelihood in red. Scatter in blue dots can be reduced by running a longer MCMC chain. The blue dots are expected to converge to the red curve from below.

B. $\Omega_m h^2$ trend

In the previous section we confirmed that there is an inconsistency between the Λ CDM model and standardisable QSOs precisely because Ω_m is not observationally a constant. Moreover, QSOs prefer larger Ω_m values than the Planck value [57], thereby alleviating the tension with independent JWST observations as explained in section II. In section II we also confirmed that increasing $\Omega_m h^2$ relative to Planck values helps alleviate the JWST anomaly. Thus, here we also look for an increasing $\Omega_m h^2$ trend in QSO data.

Previously, we fixed H_0 to the nominal value $H_0 = 70$ km/s/Mpc and allowed β to vary in order to break a degeneracy between the parameters. In this section, we fix β to a nominal value and allow H_0 to vary. We do this to ascertain whether only Ω_m varies with effective redshift or whether the combination $\Omega_m h^2$ varies. Note, while Ω_m increases from Fig. 3, it is plausible that $h := H_0/100$ decreases so that the combination $\Omega_m h^2$ remains constant. In some sense, this question is already partially addressed in Table I in [92], where it was observed that both Ω_m and β MLEs increase with effective redshift. Since $\gamma \approx 0.6 < 1$, from equation (14) it follows that increases in β with fixed H_0 are mapped to increases in H_0 with fixed β . Given that the data is the same here and there, it is easy to guarantee that H_0 increases with effective redshift, and therefore that $\Omega_m h^2$ must increase with effective redshift.

In Fig. 5 we show the profile likelihoods for $\Omega_m h^2$. To get this plot, we fixed β to the nominal value $\beta = 6.1$, so that H_0 adopts a canonical value, i. e. $H_0 \approx 70$ km/s/Mpc in the lowest redshift bin, $0 < z \leq 0.7$. Note that in this range Ω_m has a best fit value of $\Omega_m = 0.261$ from Table I. In turn, this implies $\Omega_m h^2 \approx 0.13$. In Fig. 5 we scan over $\Omega_m h^2$ in intervals of $\Delta(\Omega_m h^2) = 1$ in the range $\Omega_m h^2 \in [0, 300]$. Unfortunately, this means that there is only one point below $\Omega_m h^2 = 1$, but nevertheless if one looks closely at the plot, a peak is evident

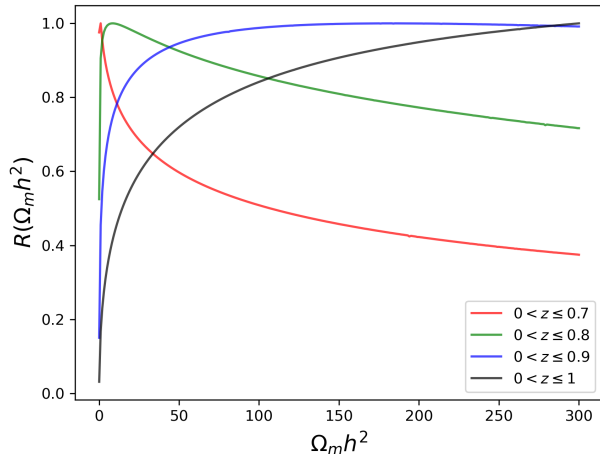


FIG. 5. Variation of profile likelihoods $R(\Omega_m h^2)$ with increasing effective redshift of the QSO sample. The Λ CDM parameter $\Omega_m h^2$ is not a constant when confronted to the QSO data.

in the red curve. Throughout, to get the curves we fixed β , but maximised the log-likelihood with respect to the parameters $(H_0, \Omega_m, \gamma, \delta)$ while imposing a constraint on the combination in $\Omega_m h^2$ through the likelihood. By scanning over the $\Omega_m h^2$ constraint in the range $\Omega_m \in [0, 300]$ we produced Fig. 5.

There are a number of lessons. First, we confirm that $\Omega_m h^2$ increases with effective redshift. This is evident in the shift in the peaks of the profiles. In particular, the red, green and blue curves are all peaked in the range $0 < \Omega_m h^2 < 300$, whereas the black curve peaks at $\Omega_m h^2 > 300$. It is evident from the profiles that the confidence intervals are large, and that the profiles may fall away to $R(\Omega_m h^2) = 0$ very gradually even for profile likelihoods peaked at larger $\Omega_m h^2$ values, despite blue and black curves disfavouring the peak of the red curve strongly. It is clear from the constrained profiles in Fig. 3 that the broad profiles in Fig. 5 are driven by an inability to constrain H_0 . This presumably is due to the considerable scatter in the QSO data and the fact that this scatter is absorbed through a relatively large intrinsic dispersion δ . The sparseness of QSOs at lower redshifts is also expected to lead to poorer constraints on H_0 . Ultimately, QSO data on its own may be good enough to constrain Ω_m but the constraints on H_0 are poor. At best, Fig. 5 appears consistent with the combination $\Omega_m h^2$ increasing with effective redshift, but the statistical significance of the trend is low. Next, we turn our attention to GRB data sets, which have fewer observables and larger intrinsic scatter, so for this reason, we focus exclusively on Ω_m , and not $\Omega_m h^2$, where already results are less conclusive in a better quality QSO data set.

V. GRB ANOMALY

In this section we repeat the analysis with GRB samples. Concretely, we study a compilation of 220 long GRBs [81]

¹² in the redshift range $0.034 \leq z \leq 8.2$ and 118 long GRBs in the redshift range $0.34 < z < 8.2$ [112]. Our interest here is exploring high redshift observables that have different systematics to QSOs. In addition, while the standardisability of QSOs has been called into question [74–80], similar tests on GRBs standardised through the Amati correlation [113] have been presented with a relatively clean bill of health [81]. More precisely, the authors of [81] claim that GRBs being standardisable, nonetheless, the full sample of 220 GRBs leads to a value of the Λ CDM parameter Ω_m that is discrepant at the $> 2\sigma$ level with the Planck- Λ CDM cosmology. We revisit this disagreement with profile likelihoods.

Here, beginning with the 220 GRB sample [81], we ask a number of questions. First, as confirmed by earlier analysis, there is a low redshift subsample of the Risaliti-Lusso QSOs [72] that recovers canonical Planck values, as claimed originally in [92] in the absence of external data sets, notably Type Ia SNe, *cf.* [71]. Thus, is there a low redshift subsample of the 220 GRB sample that recovers canonical Planck values $\Omega_m \sim 0.3$? Second, [81] imposes the conventional Ω_m bounds, $0 \leq \Omega_m \leq 1$ priors. Following the QSO analysis, we relax the bounds to identify the MLEs from the log-likelihoods. This allows us to confirm the preference of the GRB sample for larger Ω_m values. Lastly, we investigate if the profile likelihood changes with the effective redshift of the GRB sample.

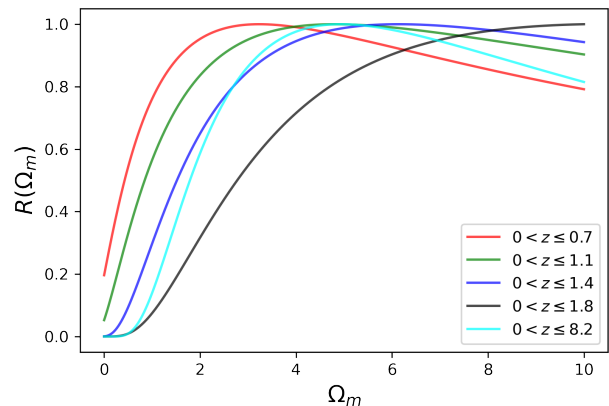


FIG. 6. Variation of profile likelihoods $R(\Omega_m)$ with increasing effective redshift of the 220 GRB sample [81]. The Λ CDM parameter Ω_m is not a constant when confronted to the GRB data.

We consider the log-likelihood

$$\ln \mathcal{L} = -\frac{1}{2} \sum_{i=1}^N \left[\frac{(\log E_{\text{iso},i} - (\beta + \gamma \log E_{\text{p},i}))^2}{s_i^2} + \ln(2\pi s_i^2) \right] \quad (19)$$

where $E_{\text{p},i}$ is the spectral peak energy and $E_{\text{iso},i}$ is the isotropic equivalent radiated energy of the i^{th} GRB, and s_i denotes the

¹²This sample is the same as the 221 GRB sample from [111] modulo the removal of a single GRB with an unreliable redshift and updating 8 GRBs.

associated error,

$$s_i^2 = \delta^2 + \left(\frac{\sigma_{S_{\text{bolo},i}}}{S_{\text{bolo},i} \ln(10)} \right)^2 + \beta^2 \left(\frac{\sigma_{E_{p,i}}}{E_{p,i} \ln(10)} \right)^2. \quad (20)$$

The data set [81] provides redshifts, z_i , $E_{p,i}$ and its error $\sigma_{E_{p,i}}$, along with the measured bolometric fluence $S_{\text{bolo},i}$ and its error $\sigma_{S_{\text{bolo},i}}$. The Λ CDM cosmological parameters (H_0 , Ω_m) enter through the luminosity distance (15), which together with $S_{\text{bolo},i}$ allows one to reconstruct $E_{\text{iso},i}$:

$$E_{\text{iso},i} = 4\pi D_L(z_i)^2 S_{\text{bolo},i} (1 + z_i)^{-1}. \quad (21)$$

This leaves us with 5 parameters, two of which are cosmological, and another 3 nuisance parameters (β , γ , δ). Once again H_0 is degenerate with β , so we set $H_0 = 70$ km/s/Mpc to remove this degeneracy and this leaves 4 parameters to be constrained. Our first check of the data set, especially the $S_{\text{bolo},i}$ entries, is to adopt Planck values (H_0 , Ω_m) = (67.34, 0.315) and confirm that one recovers Table 1 of [111]. Having performed this step, we move onto constructing the profile likelihood ratios.

Given that our GRB data set comprises a factor of 10 fewer observables compared to the QSO data, yet spans a comparable redshift range, we expect larger errors. Translated into confidence intervals, one then expects broader profile likelihoods, which necessitates relaxing our uniform prior on Ω_m to $\Omega_m \in [0, 10]$. We next break this interval up into 300 evenly spaced values of Ω_m and for each value of Ω_m we maximise the log-likelihood (19) with respect to (β , γ , δ). Throughout, we make sure that the values of (β , γ , δ) that maximise (19) are not impacted by our bounds on those parameters. For each value of Ω_m we record the maximum value of the likelihood $\mathcal{L}_{\text{max}}(\Omega_m)$, determine the global maximum of the likelihood \mathcal{L}_{max} in the range $\Omega_m \in [0, 10]$, and construct the profile likelihood ratio for $R(\Omega_m)$ in equation (18).

The result of the exercise is shown in Fig. 6, where we have constructed the profile likelihood ratios $R(\Omega_m)$ in bins of increasing effective redshift. Once again, similar to Fig. 3, we see that as the effective redshift of the sample increases, the peak of the likelihood shifts to larger Ω_m values. However, in contrast to Fig. 3, the profile likelihoods are broader so the shifts in the peak are less pronounced. That being said, inspection of the bottom left corner of the plot confirms that smaller Ω_m values, including the canonical Planck $\Omega_m \sim 0.3$ value, become steadily more disfavoured as the effective redshift of the sample increases. In Table II we provide an estimate of the 68% confidence intervals, where it is also obvious that all profile likelihood peaks inhabit the $\Omega_m > 1$ regime corresponding to negative dark energy density. We do this by integrating under the curve following equations (11) and (12), and in addition we document values of Ω_m where $\Delta\chi^2 \leq 1$. Since the curves do not exceed $\Delta\chi^2 = 1$, corresponding to $R(\Omega_m)$ values below $R(\Omega_m) = 0.607$, we are unable to determine upper bounds. It is evident that there is a considerable difference in the results, but this is expected, since the profile likelihoods are far from Gaussian, so this is a reasonable outcome. Nevertheless, the main takeaway message is that the frequentist confidence intervals for Ω_m shift to larger values

with increasing effective redshift and this can be seen from either methodology for frequentist confidence intervals. This trend continues through to $0 < z \leq 1.8$, but since the peak of the profile likelihood shifts back to smaller Ω_m values for the full sample, it is clear that the trend is not universal and it only persists at lower redshifts $z \lesssim 2$. We remind the reader that Ω_m is theoretically a constant, so its variation with effective redshift in the GRB sample [81] represents an inconsistency between the data set and the Λ CDM model.

Redshift	# GRBs	Ω_m (68%)	Ω_m ($\Delta\chi^2 \leq 1$)
$0 < z \leq 0.7$	32	$3.244^{+4.448}_{-1.839}$	$0.635 < (3.244)$
$0 < z \leq 1.1$	57	$4.816^{+4.013}_{-2.074}$	$1.137 < (4.816)$
$0 < z \leq 1.4$	90	$6.120^{+3.612}_{-2.074}$	$1.873 < (6.120)$
$0 < z \leq 1.8$	122	$5.117 < (10)$	$3.344 < (10)$
$0 < z \leq 8.2$	220	$4.950^{+3.579}_{-1.873}$	$2.074 < (4.950)$

TABLE II. The number of GRBs in redshift bins with 68% confidence intervals for Ω_m from the 220 GRB sample [81]. Ω_m best fits and confidence intervals increase with effective redshift. In the absence of an upper bound we present the profile likelihood peak in brackets.

We now attempt to assess the inconsistency between the full data set and the Planck Ω_m value. The profile likelihood ratio for the full sample appears as the cyan curve in Fig. 6. It is clear that small values of Ω_m are unlikely. To ascertain how unlikely is the Planck 1σ upper bound $\Omega_m \leq 0.322$ [57], we identify the $R(\Omega_m)$ values. We find $R(\Omega_m) \leq 0.00052$. Translated into a difference in $\Delta\chi^2$ in (18), we ascertain that the Planck values correspond to $\Delta\chi^2 \geq 15.1$. Given the GRB data, this excludes the Planck value at 99.99% confidence level corresponding to $\sim 3.9\sigma$. We can get another perspective on this number by employing our methodology from (11) and (12), where the reader should bear in mind that we have cut off the profile likelihood at $\Omega_m = 10$. We find that the Planck value is disfavoured at 99.9994% confidence interval corresponding to $\sim 4.5\sigma$. The large difference between $\sim 3.9\sigma$ and $\sim 4.5\sigma$ can be attributed to the fact that the profile likelihood is far from Gaussian. The key point here is that irrespective of the methodology, *provided one resorts to frequentist profile likelihood ratios*, there is a strong tension $> 3\sigma$ between the 220 GRB data set [81] and the Planck- Λ CDM model. In the appendix we confirm a $> 4\sigma$ tension with complementary Bayesian methods.

One puzzling outcome of the analysis is that even when we restrict GRBs to redshift ranges where Type Ia SNe and QSOs (see Fig. 3) lead to profile likelihoods peaked close to the Planck value $\Omega_m \sim 0.3$, in the sample of 220 GRBs studies in [81] this is not the case. Thus, it is interesting to change the GRB sample, and repeat the exercise. To that end, we focus on the smaller sample of 118 GRBs from [112]. The price one pays is halving the size of the GRB sample, while marginally increasing the intrinsic dispersion parameter δ , a measure of the scatter in the sample, from $\delta \sim 0.38$ to $\delta \sim 0.4$.

In Table III and Fig. 7 we show the results of the same exercise with the 118 GRB sample [112]. Despite halving the

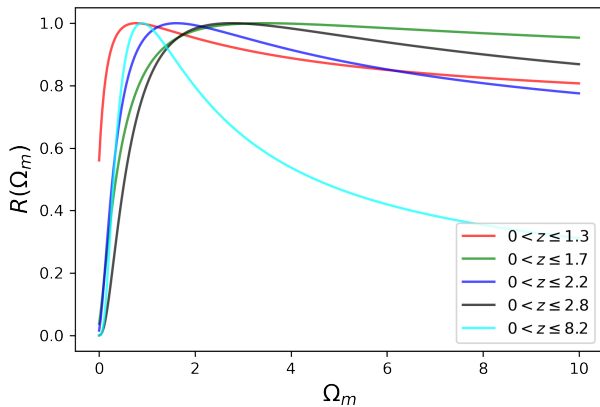


FIG. 7. Variation of profile likelihoods $R(\Omega_m)$ with increasing effective redshift of the 118 GRB sample [112]. While the data prefers large $\Omega_m \gtrsim 1$ values, in contrast to Fig. 3 and Fig. 6, Ω_m does not vary with effective redshift.

number of GRBs, once again we see that the data set has a preference for larger $\Omega_m \gtrsim 1$ values. However, in contrast to the QSO and 220 GRB samples, we no longer see a definite trend of increasing Ω_m with increasing effective redshift. However, one similarity with the 220 GRB sample in Fig. 6 is that including the high redshift GRBs $z \gtrsim 2 - 3$ pulls the Ω_m value back to lower values. This similarity is expected as GRB samples presumably possess a considerable number of high redshift GRBs in common. Thus, as is evident from Table III, GRB subsamples at intermediate redshifts show the greatest discrepancy with the Planck Ω_m value, however across the full sample, any disagreement is lower. Finally, we remark that frequentist confidence intervals based on complementary techniques lead to wildly different results, but where the profile likelihood is most Gaussian, namely for the full sample, we see that the confidence intervals show the best agreement. However, once again it is worth noting that the methodology based on (11) and (12) leads to larger confidence intervals and thus more conservative results.

Redshift	# GRBs	Ω_m (68%)	Ω_m ($\Delta\chi^2 \leq 1$)
$0 < z \leq 1.3$	19	$0.769^{+6.020}_{-0.602}$	$0.033 < (0.769)$
$0 < z \leq 1.7$	39	$3.445^{+4.849}_{-1.639}$	$0.502 < (3.445)$
$0 < z \leq 2.2$	60	$1.605^{+5.619}_{-1.003}$	$0.368 < (1.605)$
$0 < z \leq 2.8$	82	$2.776^{+4.916}_{-1.405}$	$0.669 < (2.776)$
$0 < z \leq 8.2$	118	$0.903^{+4.649}_{-0.602}$	$0.903^{+2.341}_{-0.535}$

TABLE III. The number of GRBs in redshift bins with 68% confidence intervals for Ω_m from the 118 GRB sample [112]. Ω_m best fits and confidence intervals increase with effective redshift. In the absence of an upper bound we present the profile likelihood peak in brackets.

Before leaving this section, it is good to drill down on the discrepancy between the full 118 GRB sample [112] and the

1σ Planck upper bound $\Omega_m \leq 0.322$ [57]. We find that the resulting $R(\Omega_m)$ values are $R(\Omega_m) \leq 0.502$ corresponding to $\Delta\chi^2 \geq 1.38$, which disfavors the Planck value at 76% confidence level or $\sim 1.2\sigma$. In contrast, using our methodology from (11) and (12), the 1σ Planck Ω_m upper bound appears at 58% confidence level or $\sim 0.8\sigma$. In contrast to the larger 220 GRB sample [81], where a significant $\gtrsim 4\sigma$ tension arises with Planck, in the smaller 118 GRB sample, despite large Ω_m values being favoured, the disagreement with Planck is negligible at the $\sim 1\sigma$ level.

VI. CONCLUSIONS

In this paper we have explored the synergies between existing JWST [1–8] and QSO [71, 99] anomalies. Interpreted as a problem of cosmological origin, the former anomaly can be alleviated if matter density Ω_m [68] or physical matter density $\Omega_m h^2$ [65–68] are larger than Planck values at higher redshifts. Since Ω_m and h must be constant if the Λ CDM model is correct, this is a conflict between the model and observation. We have independently confirmed these observations in this paper in section II. On the other hand, the Risaliti-Lusso QSOs are discrepant with the Planck- Λ CDM model and this discrepancy is most transparent at higher redshifts, where the luminosity distance/distance modulus falls off relative to Planck [71]. Translated into the Λ CDM cosmology, as remarked in [73, 114], this corresponds to a Universe with little or no dark energy, i. e. $\Omega_m \sim 1$.

However, this may not be the full story. In [92] it was observed that Ω_m increases with effective redshift in the QSO sample. Importantly, as we have seen in Fig. 3, QSOs recover the Planck value $\Omega_m \sim 0.3$ at lower redshifts. In this paper we have revisited the observation with profile likelihoods and confirmed that the 68% confidence intervals are shifted to larger Ω_m values as one increases the effective redshift of the sample. Moreover, profile likelihood peaks in $\Omega_m > 1$ parameter space are consistent with negative dark energy density. Since Ω_m *theoretically* must be a constant in the Λ CDM model if matter is pressureless, which incidentally is an assumption that Bayesian cosmologists need never question, *observationally* Ω_m need not be a constant. In particular, a non-constant Ω_m is either a problem with the Λ CDM model or the data set, here the Risaliti-Lusso QSO data set [72]. If the problem is on the data set side, this adds credence to claims that QSOs are not standardisable [74–80].

In section III we explained the limitations with the existing frequentist confidence interval literature and highlighted new methodology [82, 84] (see also [83]). Where the profile likelihoods were better constrained, we observed that the new methodology resulted in larger, more conservative confidence intervals than more established methodology that approximates profile likelihoods as Gaussian distributions, most recently [115, 116]. It should be obvious that given the assumptions in Wilks’ theorem [88] (recall (6)) that both methodologies show best agreement when profile likelihoods are closest to Gaussian.

However, given the question marks over QSOs as standard-

isable candles [74–80], we analysed independent GRB samples [81, 112]. For both samples, we find larger values of Ω_m than Planck expectations. Observations that GRBs prefer larger Ω_m values than Planck are widespread in the GRB literature [112, 117–120]. Moreover, we find that the larger 220 GRB sample [81] exhibits an increasing Ω_m trend with effective redshift, which is in sync with our QSO observation, but there is no hint of evolution of Ω_m in the smaller 118 GRB sample [112]. In addition, we found that both the QSO sample and 220 GRB sample showed a strong $\gtrsim 4\sigma$ tension with the Planck Ω_m value with standard frequentist methods (see appendix for Bayesian methods). Given the disagreement in GRB samples, it is imperative to revisit our methodology and results with other GRB samples, e. g. [121]. Note, as with Type Ia SNe, *uncalibrated* QSOs and GRBs can constrain Ω_m , so the goal is to identify GRB samples good enough to recover the Planck Ω_m value,¹³ especially at lower redshifts. In contrast to QSOs, even at lower redshifts, neither of the GRB samples considered in this work succeed in convincingly recovering the Planck value without resorting to large errors.

In the big picture, Planck data constrains the angular scale of the sound horizon at last scattering $\theta_* = r_*/D_M(z_*)$ almost model independently to high precision, where the scale r_* depends on physics in the early Universe and $z_* \approx 1090$. A key point here is that $D_M(z_*) := c \int_0^{z_*} 1/H(z)dz$ is a weighted sum that attributes much greater weight to lower redshifts in the matter dominated regime where $H(z)$ is smaller ($1/H(z)$ is larger). In contrast, $r_* := \int_{z_*}^{\infty} c_s(z)/H(z)dz$, where $c_s(z)$ is the speed of sound in the plasma, is also a weighted sum, but it is dominated by assumptions in the radiation sector. What this means in practice is that deviations at higher redshifts in the matter dominated regime from Planck behaviour are poorly constrained by θ_* . Admittedly, JWST observations, QSOs and GRBs, while they are relevant high redshift observables, come with considerable uncertainties. For this reason, it is prudent to turn our attention to Type Ia SNe, where analogous hints of larger Ω_m values at higher redshifts exist in the literature [92–95]. Interestingly, two recent SNe sample have favoured values of Ω_m larger than Planck [122, 123], and it is evident that the DES SNe sample [123] has a high effective redshift. We plan on reporting on the DES SNe sample soon.

ACKNOWLEDGMENTS

We would like to thank Stephen Appleby, Giacomo Galoni, Adrià Gómez-Valent, Elisabeta Lusso and Saeed Pourojahi for discussions on JWST anomalies, profile likelihoods, QSOs, GRBs, etc. We thank Orlando Luongo, Marco Muccino and Bharat Ratra for comments on a preliminary draft. We thank Dominik Schwarz, Yvonne Wong and an anonymous EPJC referee for inspiring section III on frequentist

¹³One can recover the Planck value from QSOs over extensive redshift ranges [100], but one does so by correcting or editing the raw data to promote (13) to a relation intrinsic to QSO by removing by ansatz correlations between the UV and X-ray luminosities and redshift.

confidence intervals. This article/publication is based upon work from COST Action CA21136 – “Addressing observational tensions in cosmology with systematics and fundamental physics (CosmoVerse)”, supported by COST (European Cooperation in Science and Technology). LY is supported by an appointment to the YST Program at the APCTP through the Science and Technology Promotion Fund and Lottery Fund of the Korean Government.

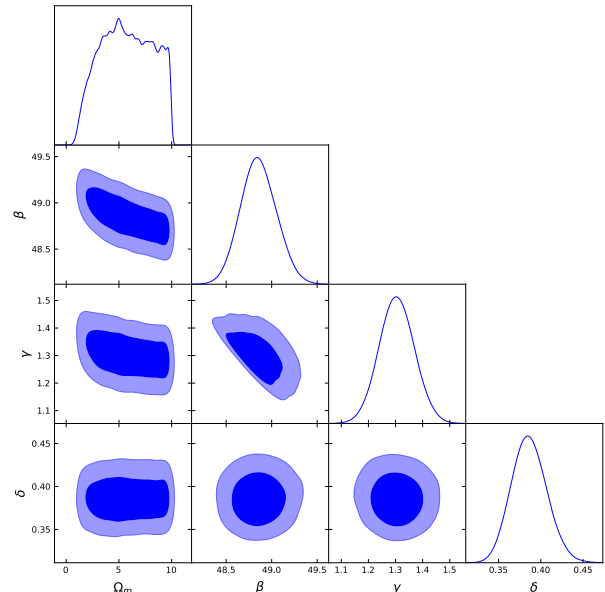


FIG. 8. MCMC posteriors for the 220 GRB data set [81] fitted to the Λ CDM model with H_0 fixed to $H_0 = 70$ km/s/Mpc to break a degeneracy.

Appendix A: MCMC confirmation of GRB tension

The analysis in the text has led to strong $\gtrsim 4\sigma$ tensions between GRB and QSO samples with Planck CMB data on the assumption that the Λ CDM model is correct. In this section, we confirm that one would arrive at the same conclusions with MCMC analysis. In Fig. 8 we show the MCMC posteriors for the data set of 220 GRBs [81], where we have made use of *emcee* [124] and *GetDist* [125]. The Ω_m posterior should be compared with the cyan curve from Fig. 6. Both plots demonstrate a peak at $\Omega_m \sim 5$ with a sharp fall off towards smaller Ω_m values and a gradual fall off towards larger Ω_m values. Unfortunately, the tension with the Planck value is unclear from the corner plot.

In Fig. 9 we plot a histogram of the 31,980 Ω_m values from the MCMC chain, which confirms that we encounter no values of Ω_m smaller than the 1σ upper bound on the Planck value $\Omega_m \leq 0.322$ highlighted in red. The lowest value we find is $\Omega_m \sim 0.455$. Removing non-unique points in $(\Omega_m, \beta, \gamma, \delta)$ parameter space from the MCMC chain, the number of unique configurations is 31,933. Thus, the probability p of getting a value of Ω_m consistent with Planck within 1σ is conserva-

tively less than $p < 1/31933$, which points to a tension between the GRB data set and Planck data that is bounded below at the 99.997% confidence level or 4σ .

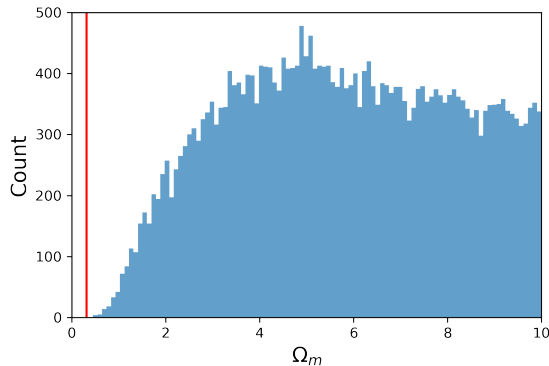


FIG. 9. A histogram of 31,980 Ω_m values from the MCMC chain for the 220 GRB data set [81] fitted to the Λ CDM model with H_0 fixed to $H_0 = 70$ km/s/Mpc. The Planck 68% confidence interval is shown in red.

One could more accurately determine the tension from the MCMC chain, but it is clear that one needs to run a chain long enough to encounter the Planck value or its 1σ upper bound. What is important here is that we arrived at 3.9σ tension through a difference in the χ^2 in section V, but it is clear from our MCMC analysis that this number is a lower bound. In principle, one could run a very long MCMC chain to see whether the tension as ascertained by MCMC is closer to the 4.5σ we found with methodology based on equations (11) and (12). This would require an MCMC chain approximately 10 times as long with $\sim 300,000$ entries. Given that the MCMC chain converges with $\sim 10,000$ entries, this represents a poor use of computation for relatively little gain. The main take-away from this section is that the 3.9σ tension between the GRB data set and Planck is recovered with Bayesian methodology based on MCMC, modulo the fact that long MCMC chains are required.

-
- [1] N. J. Adams, C. J. Conselice, L. Ferreira, D. Austin, J. A. A. Trussler, I. Juodžbalis, S. M. Wilkins, J. Caruana, P. Dayal, A. Verma, and A. P. Vijayan, Discovery and properties of ultra-high redshift galaxies ($9 \leq z \leq 12$) in the JWST ERO SMACS 0723 Field, *Monthly Notices of the Royal Astronomical Society* **518**, 4755 (2022), <https://academic.oup.com/mnras/article-pdf/518/3/4755/47749914/stac3347.pdf>.
- [2] I. Labbé *et al.*, A population of red candidate massive galaxies ~ 600 Myr after the Big Bang, *Nature* **616**, 266 (2023), [arXiv:2207.12446](https://arxiv.org/abs/2207.12446) [astro-ph.GA].
- [3] M. Castellano *et al.*, Early Results from GLASS-JWST. XIX. A High Density of Bright Galaxies at $z \approx 10$ in the A2744 Region, *Astrophys. J. Lett.* **948**, L14 (2023), [arXiv:2212.06666](https://arxiv.org/abs/2212.06666) [astro-ph.GA].
- [4] S. L. Finkelstein, M. B. Bagley, H. C. Ferguson, S. M. Wilkins, J. S. Kartaltepe, C. Papovich, L. Y. A. Yung, P. Arrabal Haro, P. Behroozi, M. Dickinson, D. D. Kocevski, A. M. Koekoemoer, R. L. Larson, A. Le Bail, A. M. Morales, P. G. Pérez-González, D. Burgarella, R. Davé, M. Hirschmann, R. S. Somerville, S. Wuyts, V. Bromm, C. M. Casey, A. Fontana, S. Fujimoto, J. P. Gardner, M. Giavalisco, A. Grazian, N. A. Grogan, N. P. Hathi, T. A. Hutchison, S. W. Jha, S. Jagee, L. J. Kewley, A. Kirkpatrick, A. S. Long, J. M. Lotz, L. Pentericci, J. D. R. Pierel, N. Pirzkal, S. Ravindranath, R. E. Ryan, J. R. Trump, G. Yang, R. Bhatawdekar, L. Bisigello, V. Buat, A. Calabrò, M. Castellano, N. J. Cleri, M. C. Cooper, D. Croton, E. Daddi, A. Dekel, D. Elbaz, M. Franco, E. Gawiser, B. W. Holwerda, M. Huertas-Company, A. E. Jaskot, G. C. K. Leung, R. A. Lucas, B. Mobasher, V. Pandya, S. Tacchella, B. J. Weiner, and J. A. Zavala, Ceers key paper. i. an early look into the first 500 myr of galaxy formation with jwst, *The Astrophysical Journal Letters* **946**, L13 (2023).
- [5] H. Atek, M. Shuntov, L. J. Furtak, J. Richard, J.-P. Kneib, G. Mahler, A. Zitrin, H. J. McCracken, S. Charlot, J. Chevalard, and I. Chemerynska, Revealing galaxy candidates out to $z \approx 16$ with JWST observations of the lensing cluster SMACS0723, *mnras* **519**, 1201 (2023), [arXiv:2207.12338](https://arxiv.org/abs/2207.12338) [astro-ph.GA].
- [6] C. T. Donnan, D. J. McLeod, J. S. Dunlop, R. J. McLure, A. C. Carnall, R. Begley, F. Cullen, M. L. Hamadouche, R. A. A. Bowler, D. Magee, H. J. McCracken, B. Milvang-Jensen, A. Moneti, and T. Targett, The evolution of the galaxy UV luminosity function at redshifts $z \leq 8 - 15$ from deep JWST and ground-based near-infrared imaging, *mnras* **518**, 6011 (2023), [arXiv:2207.12356](https://arxiv.org/abs/2207.12356) [astro-ph.GA].
- [7] R. P. Naidu, P. A. Oesch, P. van Dokkum, E. J. Nelson, K. A. Suess, G. Brammer, K. E. Whitaker, G. Illingworth, R. Bouwens, S. Tacchella, J. Matthee, N. Allen, R. Bezanson, C. Conroy, I. Labbé, J. Leja, E. Leonova, D. Magee, S. H. Price, D. J. Setton, V. Strait, M. Stefanon, S. Toft, J. R. Weaver, and A. Weibel, Two Remarkably Luminous Galaxy Candidates at $z \approx 10-12$ Revealed by JWST, *apjl* **940**, L14 (2022), [arXiv:2207.09434](https://arxiv.org/abs/2207.09434) [astro-ph.GA].
- [8] H. Yan, Z. Ma, C. Ling, C. Cheng, and J.-S. Huang, First Batch of $z \approx 11-20$ Candidate Objects Revealed by the James Webb Space Telescope Early Release Observations on SMACS 0723-73, *apjl* **942**, L9 (2023), [arXiv:2207.11558](https://arxiv.org/abs/2207.11558) [astro-ph.GA].
- [9] C. C. Lovell, I. Harrison, Y. Harikane, S. Tacchella, and S. M. Wilkins, Extreme value statistics of the halo and stellar mass distributions at high redshift: are JWST results in tension with Λ CDM?, *Mon. Not. Roy. Astron. Soc.* **518**, 2511 (2022), [arXiv:2208.10479](https://arxiv.org/abs/2208.10479) [astro-ph.GA].
- [10] S. Fujimoto *et al.*, ALMA FIR View of Ultra-high-redshift Galaxy Candidates at $z \approx 11-17$: Blue Monsters or Low- z Red Interlopers?, *Astrophys. J.* **955**, 130 (2023), [arXiv:2211.03896](https://arxiv.org/abs/2211.03896) [astro-ph.GA].
- [11] F. Prada, P. Behroozi, T. Ishiyama, A. Klypin, and E. Pérez, Confirmation of the standard cosmological model from red

- massive galaxies ~ 600 myr after the big bang (2023), [arXiv:2304.11911 \[astro-ph.GA\]](#).
- [12] Y. Chen, H. J. Mo, and K. Wang, Massive dark matter haloes at high redshift: implications for observations in the JWST era, *Mon. Not. Roy. Astron. Soc.* **526**, 2542 (2023), [arXiv:2304.13890 \[astro-ph.GA\]](#).
- [13] M. Forconi, Ruchika, A. Melchiorri, O. Mena, and N. Menci, Do the early galaxies observed by JWST disagree with Planck's CMB polarization measurements?, *JCAP* **10**, 012, [arXiv:2306.07781 \[astro-ph.CO\]](#).
- [14] C. L. Steinhardt, A. Sneppen, T. Clausen, H. Katz, M. P. Rey, and J. Stahlschmidt, The highest-redshift balmer breaks as a test of λ cdm (2023), [arXiv:2305.15459 \[astro-ph.GA\]](#).
- [15] A. Vikaeus, E. Zackrisson, S. Wilkins, A. Nabizadeh, V. Kokorev, Abdurrouf, L. D. Bradley, D. Coe, P. Dayal, and M. Ricotti, To be, or not to be: Balmer breaks in high-z galaxies with jwst (2023), [arXiv:2309.02504 \[astro-ph.GA\]](#).
- [16] B. E. Robertson *et al.*, Identification and properties of intense star-forming galaxies at redshifts $z > 10$, *Nature Astron.* **7**, 611 (2023), [arXiv:2212.04480 \[astro-ph.GA\]](#).
- [17] P. Parashari and R. Laha, Primordial power spectrum in light of JWST observations of high redshift galaxies, *Mon. Not. Roy. Astron. Soc.* **526**, L63 (2023), [arXiv:2305.00999 \[astro-ph.CO\]](#).
- [18] N. Sabti, J. B. Muñoz, and M. Kamionkowski, Insights from HST into Ultramassive Galaxies and Early-Universe Cosmology, *Phys. Rev. Lett.* **132**, 061002 (2024), [arXiv:2305.07049 \[astro-ph.CO\]](#).
- [19] A. Pallottini and A. Ferrara, Stochastic star formation in early galaxies: Implications for the James Webb Space Telescope, *Astron. Astrophys.* **677**, L4 (2023), [arXiv:2307.03219 \[astro-ph.GA\]](#).
- [20] M. V. Tkachev, S. V. Pilipenko, E. V. Mikheeva, and V. N. Lukash, Excess of high-z galaxies as a test for bumpy power spectrum of density perturbations, *Mon. Not. Roy. Astron. Soc.* **527**, 1381 (2023), [arXiv:2307.13774 \[astro-ph.CO\]](#).
- [21] Y.-Y. Wang, L. Lei, G.-W. Yuan, and Y.-Z. Fan, Modeling the JWST High-redshift Galaxies with a General Formation Scenario and the Consistency with the Λ CDM Model, *Astrophys. J. Lett.* **954**, L48 (2023), [arXiv:2307.12487 \[astro-ph.GA\]](#).
- [22] J. Wang, Z. Huang, L. Huang, and J. Liu, Quantifying the tension between cosmological models and jwst red candidate massive galaxies (2023), [arXiv:2311.02866 \[astro-ph.CO\]](#).
- [23] K. Inayoshi and K. Ichikawa, Birth of rapidly spinning, overmassive black holes in the early universe (2024), [arXiv:2402.14706 \[astro-ph.GA\]](#).
- [24] J. Jeon, V. Bromm, B. Liu, and S. L. Finkelstein, Physical pathways for jwst-observed supermassive black holes in the early universe (2024), [arXiv:2402.18773 \[astro-ph.GA\]](#).
- [25] B. Liu and V. Bromm, Accelerating Early Massive Galaxy Formation with Primordial Black Holes, *Astrophys. J. Lett.* **937**, L30 (2022), [arXiv:2208.13178 \[astro-ph.CO\]](#).
- [26] H.-L. Huang, Y. Cai, J.-Q. Jiang, J. Zhang, and Y.-S. Piao, Supermassive primordial black holes in multiverse: for nano-hertz gravitational wave and high-redshift jwst galaxies (2023), [arXiv:2306.17577 \[gr-qc\]](#).
- [27] Y. Gouttenoire, S. Trifinopoulos, G. Valogiannis, and M. Vavvaselaer, Scrutinizing the primordial black holes interpretation of pta gravitational waves and jwst early galaxies (2023), [arXiv:2307.01457 \[astro-ph.CO\]](#).
- [28] P. Ralegankar, M. Pavičević, and M. Viel, Primordial magnetic fields: consistent initial conditions and impact on high-z structures (2024), [arXiv:2402.14079 \[astro-ph.CO\]](#).
- [29] S. Hirano and N. Yoshida, Early Structure Formation from Primordial Density Fluctuations with a Blue, Tilted Power Spectrum: High-redshift Galaxies, *Astrophys. J.* **963**, 2 (2024), [arXiv:2306.11993 \[astro-ph.GA\]](#).
- [30] H. Jiao, R. Brandenberger, and A. Refregier, Early structure formation from cosmic string loops in light of early JWST observations, *Phys. Rev. D* **108**, 043510 (2023), [arXiv:2304.06429 \[astro-ph.CO\]](#).
- [31] Z. Wang, L. Lei, H. Jiao, L. Feng, and Y.-Z. Fan, The nanohertz stochastic gravitational wave background from cosmic string loops and the abundant high redshift massive galaxies, *Sci. China Phys. Mech. Astron.* **66**, 120403 (2023), [arXiv:2306.17150 \[astro-ph.HE\]](#).
- [32] H. Jiao, R. Brandenberger, and A. Refregier, N-body simulation of early structure formation from cosmic string loops (2024), [arXiv:2402.06235 \[astro-ph.CO\]](#).
- [33] U. Maio and M. Viel, JWST high-redshift galaxy constraints on warm and cold dark matter models, *Astron. Astrophys.* **672**, A71 (2023), [arXiv:2211.03620 \[astro-ph.CO\]](#).
- [34] Y. Gong, B. Yue, Y. Cao, and X. Chen, Fuzzy Dark Matter as a Solution to Reconcile the Stellar Mass Density of High-z Massive Galaxies and Reionization History, *Astrophys. J.* **947**, 28 (2023), [arXiv:2209.13757 \[astro-ph.CO\]](#).
- [35] G. Hütsi, M. Raidal, J. Urrutia, V. Vaskonen, and H. Veermäe, Did JWST observe imprints of axion miniclusters or primordial black holes?, *Phys. Rev. D* **107**, 043502 (2023), [arXiv:2211.02651 \[astro-ph.CO\]](#).
- [36] M. Haslbauer, P. Kroupa, A. H. Zonoozi, and H. Haghi, Has JWST Already Falsified Dark-matter-driven Galaxy Formation?, *Astrophys. J. Lett.* **939**, L31 (2022), [arXiv:2210.14915 \[astro-ph.GA\]](#).
- [37] G. Domènech, D. Inman, A. Kusenko, and M. Sasaki, Halo formation from Yukawa forces in the very early Universe, *Phys. Rev. D* **108**, 103543 (2023), [arXiv:2304.13053 \[astro-ph.CO\]](#).
- [38] H. Lin, Y. Gong, B. Yue, and X. Chen, Implications of the Stellar Mass Density of High-z Massive Galaxies from JWST on Warm Dark Matter, *Res. Astron. Astrophys.* **24**, 015009 (2024), [arXiv:2306.05648 \[astro-ph.CO\]](#).
- [39] S. Bird, C.-F. Chang, Y. Cui, and D. Yang, Enhanced early galaxy formation in jwst from axion dark matter? (2023), [arXiv:2307.10302 \[hep-ph\]](#).
- [40] Z. Davari, A. Ashoorioon, and K. Rezazadeh, Spherical collapse approach for non-standard cold dark matter models and enhanced early galaxy formation in jwst (2023), [arXiv:2311.15083 \[astro-ph.CO\]](#).
- [41] P. Santini, N. Menci, and M. Castellano, CONSTRAINTS ON DARK ENERGY FROM THE ABUNDANCE OF MASSIVE GALAXIES, *Frascati Phys. Ser.* **74**, 239 (2022), [arXiv:2301.03892 \[astro-ph.CO\]](#).
- [42] N. Menci, M. Castellano, P. Santini, E. Merlin, A. Fontana, and F. Shankar, High-redshift Galaxies from Early JWST Observations: Constraints on Dark Energy Models, *Astrophys. J. Lett.* **938**, L5 (2022), [arXiv:2208.11471 \[astro-ph.CO\]](#).
- [43] D. Wang and Y. Liu, Jwst high redshift galaxy observations have a strong tension with planck cmb measurements (2023), [arXiv:2301.00347 \[astro-ph.CO\]](#).
- [44] P. Wang, B.-Y. Su, L. Zu, Y. Yang, and L. Feng, Exploring the dark energy equation of state with jwst (2023), [arXiv:2307.11374 \[astro-ph.CO\]](#).
- [45] S. A. Adil, U. Mukhopadhyay, A. A. Sen, and S. Vagnozzi, Dark energy in light of the early JWST observations: case for a negative cosmological constant?, *JCAP* **10**, 072, [arXiv:2307.12763 \[astro-ph.CO\]](#).
- [46] N. Menci, S. A. Adil, U. Mukhopadhyay, A. A. Sen, and

- S. Vagnozzi, Negative cosmological constant in the dark energy sector: tests from jwst photometric and spectroscopic observations of high-redshift galaxies (2024), [arXiv:2401.12659 \[astro-ph.CO\]](#).
- [47] F. Melia, The cosmic timeline implied by the JWST high-redshift galaxies, *Mon. Not. Roy. Astron. Soc.* **521**, L85 (2023), [arXiv:2302.10103 \[astro-ph.CO\]](#).
- [48] S. S. Binici, C. Deliduman, and F. Şakir Dilsiz, The ages of the oldest astrophysical objects in an ellipsoidal universe (2024), [arXiv:2402.16646 \[astro-ph.CO\]](#).
- [49] M. Lopez-Corredoira, F. Melia, J. J. Wei, and C. Y. Gao, Age of massive galaxies at redshift 8 (2024), [arXiv:2405.12665 \[astro-ph.CO\]](#).
- [50] B. W. Keller, F. Munshi, M. Trebitsch, and M. Tremmel, Can Cosmological Simulations Reproduce the Spectroscopically Confirmed Galaxies Seen at $z \geq 10$?, *Astrophys. J. Lett.* **943**, L28 (2023), [arXiv:2212.12804 \[astro-ph.GA\]](#).
- [51] G. Desprez, N. S. Martis, Y. Asada, M. Sawicki, C. J. Willott, A. Muzzin, R. G. Abraham, M. Bradač, G. Brammer, V. Estrada-Carpenter, K. G. Iyer, J. Matharu, L. Mowla, G. Noirot, G. T. E. Sarrouh, V. Strait, R. Gledhill, and G. Rihtaršič, Λ CDM not dead yet: massive high- z Balmer break galaxies are less common than previously reported, [arXiv e-prints](#), [arXiv:2310.03063 \(2023\)](#), [arXiv:2310.03063 \[astro-ph.GA\]](#).
- [52] G. Sun, C.-A. Faucher-Giguère, C. C. Hayward, X. Shen, A. Wetzel, and R. K. Cochrane, Bursty Star Formation Naturally Explains the Abundance of Bright Galaxies at Cosmic Dawn, *Astrophys. J. Lett.* **955**, L35 (2023), [arXiv:2307.15305 \[astro-ph.GA\]](#).
- [53] J. McCaffrey, S. Hardin, J. H. Wise, and J. A. Regan, No tension: Jwst galaxies at $z > 10$ consistent with cosmological simulations, *The Open Journal of Astrophysics* **6**, 10.21105/astro.2304.13755 (2023).
- [54] E. Di Valentino, O. Mena, S. Pan, L. Visinelli, W. Yang, A. Melchiorri, D. F. Mota, A. G. Riess, and J. Silk, In the realm of the Hubble tension—a review of solutions, *Class. Quant. Grav.* **38**, 153001 (2021), [arXiv:2103.01183 \[astro-ph.CO\]](#).
- [55] L. Perivolaropoulos and F. Skara, Challenges for Λ CDM: An update, *New Astron. Rev.* **95**, 101659 (2022), [arXiv:2105.05208 \[astro-ph.CO\]](#).
- [56] E. Abdalla *et al.*, Cosmology intertwined: A review of the particle physics, astrophysics, and cosmology associated with the cosmological tensions and anomalies, *JHEAp* **34**, 49 (2022), [arXiv:2203.06142 \[astro-ph.CO\]](#).
- [57] N. Aghanim *et al.* (Planck), Planck 2018 results. VI. Cosmological parameters, *Astron. Astrophys.* **641**, A6 (2020), [Erratum: *Astron. Astrophys.* 652, C4 (2021)], [arXiv:1807.06209 \[astro-ph.CO\]](#).
- [58] L. Knox and M. Millea, Hubble constant hunter’s guide, *Phys. Rev. D* **101**, 043533 (2020), [arXiv:1908.03663 \[astro-ph.CO\]](#).
- [59] V. Poulin, T. L. Smith, T. Karwal, and M. Kamionkowski, Early Dark Energy Can Resolve The Hubble Tension, *Phys. Rev. Lett.* **122**, 221301 (2019), [arXiv:1811.04083 \[astro-ph.CO\]](#).
- [60] P. Agrawal, F.-Y. Cyr-Racine, D. Pinner, and L. Randall, Rock ‘n’ roll solutions to the Hubble tension, *Phys. Dark Univ.* **42**, 101347 (2023), [arXiv:1904.01016 \[astro-ph.CO\]](#).
- [61] M.-X. Lin, G. Benevento, W. Hu, and M. Raveri, Acoustic Dark Energy: Potential Conversion of the Hubble Tension, *Phys. Rev. D* **100**, 063542 (2019), [arXiv:1905.12618 \[astro-ph.CO\]](#).
- [62] F. Niedermann and M. S. Sloth, New early dark energy, *Phys. Rev. D* **103**, L041303 (2021), [arXiv:1910.10739 \[astro-ph.CO\]](#).
- [63] G. Ye and Y.-S. Piao, Is the Hubble tension a hint of AdS phase around recombination?, *Phys. Rev. D* **101**, 083507 (2020), [arXiv:2001.02451 \[astro-ph.CO\]](#).
- [64] V. Poulin, T. L. Smith, and T. Karwal, The Ups and Downs of Early Dark Energy solutions to the Hubble tension: A review of models, hints and constraints circa 2023, *Phys. Dark Univ.* **42**, 101348 (2023), [arXiv:2302.09032 \[astro-ph.CO\]](#).
- [65] M. Boylan-Kolchin, Stress testing Λ CDM with high-redshift galaxy candidates, *Nature Astron.* **7**, 731 (2023), [arXiv:2208.01611 \[astro-ph.CO\]](#).
- [66] S. S. McGaugh, Discord in Concordance Cosmology and Anomalously Massive Early Galaxies, *Universe* **10**, 48 (2024), [arXiv:2312.03127 \[astro-ph.CO\]](#).
- [67] W. Liu, H. Zhan, Y. Gong, and X. Wang, Can early dark energy be probed by the high-redshift galaxy abundance? (2024), [arXiv:2402.14339 \[astro-ph.CO\]](#).
- [68] M. Forconi, W. Giarè, O. Mena, Ruchika, E. D. Valentino, A. Melchiorri, and R. C. Nunes, A double take on early and interacting dark energy from jwst (2023), [arXiv:2312.11074 \[astro-ph.CO\]](#).
- [69] M. H. P. M. van Putten, The Fast and Furious in JWST high- z galaxies, *Phys. Dark Univ.* **43**, 101417 (2024), [arXiv:2312.16692 \[astro-ph.CO\]](#).
- [70] G. Risaliti and E. Lusso, A Hubble Diagram for Quasars, *Astrophys. J.* **815**, 33 (2015), [arXiv:1505.07118 \[astro-ph.CO\]](#).
- [71] G. Risaliti and E. Lusso, Cosmological constraints from the Hubble diagram of quasars at high redshifts, *Nature Astron.* **3**, 272 (2019), [arXiv:1811.02590 \[astro-ph.CO\]](#).
- [72] E. Lusso *et al.*, Quasars as standard candles III. Validation of a new sample for cosmological studies, *Astron. Astrophys.* **642**, A150 (2020), [arXiv:2008.08586 \[astro-ph.GA\]](#).
- [73] T. Yang, A. Banerjee, and E. Ó Colgáin, Cosmography and flat Λ CDM tensions at high redshift, *Phys. Rev. D* **102**, 123532 (2020), [arXiv:1911.01681 \[astro-ph.CO\]](#).
- [74] N. Khadka and B. Ratra, Using quasar X-ray and UV flux measurements to constrain cosmological model parameters, *Mon. Not. Roy. Astron. Soc.* **497**, 263 (2020), [arXiv:2004.09979 \[astro-ph.CO\]](#).
- [75] N. Khadka and B. Ratra, Determining the range of validity of quasar X-ray and UV flux measurements for constraining cosmological model parameters, *Mon. Not. Roy. Astron. Soc.* **502**, 6140 (2021), [arXiv:2012.09291 \[astro-ph.CO\]](#).
- [76] N. Khadka and B. Ratra, Do quasar X-ray and UV flux measurements provide a useful test of cosmological models?, *Mon. Not. Roy. Astron. Soc.* **510**, 2753 (2022), [arXiv:2107.07600 \[astro-ph.CO\]](#).
- [77] N. Khadka, M. Zajaček, R. Prince, S. Panda, B. Czerny, M. L. Martínez-Aldama, V. K. Jaiswal, and B. Ratra, Quasar UV/X-ray relation luminosity distances are shorter than reverberation-measured radius–luminosity relation luminosity distances, *Mon. Not. Roy. Astron. Soc.* **522**, 1247 (2023), [arXiv:2212.10483 \[astro-ph.CO\]](#).
- [78] J. Singal, S. Mutchnick, and V. Petrosian, The X-Ray Luminosity Function Evolution of Quasars and the Correlation between the X-Ray and Ultraviolet Luminosities, *Astrophys. J.* **932**, 111 (2022), [arXiv:2203.13374 \[astro-ph.CO\]](#).
- [79] V. Petrosian, J. Singal, and S. Mutchnick, Can the Distance-Redshift Relation be Determined from Correlations between Luminosities?, *Astrophys. J. Lett.* **935**, L19 (2022), [arXiv:2205.07981 \[astro-ph.CO\]](#).
- [80] M. Zajaček, B. Czerny, N. Khadka, M. L. Martínez-Aldama, R. Prince, S. Panda, and B. Ratra, Effect of Extinction on Quasar Luminosity Distances Determined from UV and X-

- Ray Flux Measurements, *Astrophys. J.* **961**, 229 (2024), [arXiv:2305.08179 \[astro-ph.GA\]](#).
- [81] S. Cao and B. Ratra, Testing the standardizability of, and deriving cosmological constraints from, a new amati-correlated gamma-ray burst data compilation (2024), [arXiv:2404.08697 \[astro-ph.CO\]](#).
- [82] A. Gómez-Valent, Fast test to assess the impact of marginalization in Monte Carlo analyses and its application to cosmology, *Phys. Rev. D* **106**, 063506 (2022), [arXiv:2203.16285 \[astro-ph.CO\]](#).
- [83] L. Herold, E. G. M. Ferreira, and E. Komatsu, New Constraint on Early Dark Energy from Planck and BOSS Data Using the Profile Likelihood, *Astrophys. J. Lett.* **929**, L16 (2022), [arXiv:2112.12140 \[astro-ph.CO\]](#).
- [84] E. O. Colgáin, S. Pourojaghi, M. M. Sheikh-Jabbari, and D. Sherwin, MCMC Marginalisation Bias and Λ CDM tensions (2023), [arXiv:2307.16349 \[astro-ph.CO\]](#).
- [85] R. K. Sheth and G. Tormen, Large scale bias and the peak background split, *Mon. Not. Roy. Astron. Soc.* **308**, 119 (1999), [arXiv:astro-ph/9901122](#).
- [86] O. Akarsu, E. Ó Colgáin, A. A. Sen, and M. M. Sheikh-Jabbari, Λ cdm tensions: Localising missing physics through consistency checks (2024), [arXiv:2402.04767 \[astro-ph.CO\]](#).
- [87] R. Trotta, Bayesian Methods in Cosmology (2017) [arXiv:1701.01467 \[astro-ph.CO\]](#).
- [88] S. S. Wilks, The Large-Sample Distribution of the Likelihood Ratio for Testing Composite Hypotheses, *The Annals of Mathematical Statistics* **9**, 60 (1938).
- [89] G. J. Feldman and R. D. Cousins, A Unified approach to the classical statistical analysis of small signals, *Phys. Rev. D* **57**, 3873 (1998), [arXiv:physics/9711021](#).
- [90] G. Galloni, S. Henrot-Versillé, and M. Tristram, Robust constraints on tensor perturbations from cosmological data: a comparative analysis from Bayesian and frequentist perspectives, [arXiv e-prints](#), [arXiv:2405.04455 \(2024\)](#), [arXiv:2405.04455 \[astro-ph.CO\]](#).
- [91] T. Karwal, Y. Patel, A. Bartlett, V. Poulin, T. L. Smith, and D. N. Pfeffer, Procoli: Profiles of cosmological likelihoods (2024), [arXiv:2401.14225 \[astro-ph.CO\]](#).
- [92] E. Ó Colgáin, M. M. Sheikh-Jabbari, R. Solomon, G. Bargiacchi, S. Capozziello, M. G. Dainotti, and D. Stojkovic, Revealing intrinsic flat Λ CDM biases with standardizable candles, *Phys. Rev. D* **106**, L041301 (2022), [arXiv:2203.10558 \[astro-ph.CO\]](#).
- [93] E. Ó Colgáin, M. M. Sheikh-Jabbari, R. Solomon, M. G. Dainotti, and D. Stojkovic, Putting flat Λ CDM in the (Redshift) bin, *Phys. Dark Univ.* **44**, 101464 (2024), [arXiv:2206.11447 \[astro-ph.CO\]](#).
- [94] E. Pastén and V. H. Cárdenas, Testing Λ CDM cosmology in a binned universe: Anomalies in the deceleration parameter, *Phys. Dark Univ.* **40**, 101224 (2023), [arXiv:2301.10740 \[astro-ph.CO\]](#).
- [95] M. Malekjani, R. M. Conville, E. O. Colgáin, S. Pourojaghi, and M. M. Sheikh-Jabbari, On redshift evolution and negative dark energy density in Pantheon + Supernovae, *Eur. Phys. J. C* **84**, 317 (2024), [arXiv:2301.12725 \[astro-ph.CO\]](#).
- [96] E. Lusso and G. Risaliti, Quasars as standard candles I: The physical relation between disc and coronal emission, *Astron. Astrophys.* **602**, A79 (2017), [arXiv:1703.05299 \[astro-ph.HE\]](#).
- [97] A. Kubota and C. Done, A physical model of the broad-band continuum of AGN and its implications for the UV/X relation and optical variability, *Mon. Not. Roy. Astron. Soc.* **480**, 1247 (2018), [arXiv:1804.00171 \[astro-ph.HE\]](#).
- [98] R. Arcodia, A. Merloni, K. Nandra, and G. Ponti, Testing the disk-corona interplay in radiatively-efficient broad-line AGN, *Astron. Astrophys.* **628**, A135 (2019), [arXiv:1907.10069 \[astro-ph.HE\]](#).
- [99] E. Lusso, E. Piedipalumbo, G. Risaliti, M. Paolillo, S. Bisogni, E. Nardini, and L. Amati, Tension with the flat Λ CDM model from a high-redshift Hubble diagram of supernovae, quasars, and gamma-ray bursts, *Astron. Astrophys.* **628**, L4 (2019), [arXiv:1907.07692 \[astro-ph.CO\]](#).
- [100] M. G. Dainotti, G. Bardiacchi, A. L. Lenart, S. Capozziello, E. Ó Colgáin, R. Solomon, D. Stojkovic, and M. M. Sheikh-Jabbari, Quasar Standardization: Overcoming Selection Biases and Redshift Evolution, *Astrophys. J.* **931**, 106 (2022), [arXiv:2203.12914 \[astro-ph.HE\]](#).
- [101] M. G. Dainotti, A. L. Lenart, M. G. Yengejeh, S. Chakraborty, N. Fraija, E. Di Valentino, and G. Montani, A new binning method to choose a standard set of Quasars, *Phys. Dark Univ.* **44**, 101428 (2024), [arXiv:2401.12847 \[astro-ph.HE\]](#).
- [102] B. Trefoloni, E. Lusso, E. Nardini, G. Risaliti, A. Marconi, G. Bargiacchi, A. Sacchi, and M. Signorini, Quasars as standard candles vi: spectroscopic validation of the cosmological sample (2024), [arXiv:2404.07205 \[astro-ph.GA\]](#).
- [103] M. Moresco *et al.*, Unveiling the Universe with emerging cosmological probes, *Living Rev. Rel.* **25**, 6 (2022), [arXiv:2201.07241 \[astro-ph.CO\]](#).
- [104] B. Czerny *et al.*, Accretion disks, quasars and cosmology: meandering towards understanding, *Astrophys. Space Sci.* **368**, 8 (2023), [arXiv:2209.06563 \[astro-ph.GA\]](#).
- [105] C. Vignali, W. N. Brandt, and D. P. Schneider, X-ray emission from radio - quiet quasars in the SDSS Early Data Release. The Alpha(ox) dependence upon UV luminosity, *Astron. J.* **125**, 433 (2003), [arXiv:astro-ph/0211125](#).
- [106] D. W. Just, W. N. Brandt, O. Shemmer, A. T. Steffen, D. P. Schneider, G. Chartas, and G. P. Garmire, The X-ray Properties of the Most-Luminous Quasars from the Sloan Digital Sky Survey, *Astrophys. J.* **665**, 1004 (2007), [arXiv:0705.3059 \[astro-ph\]](#).
- [107] E. Lusso, A. Comastri, C. Vignali, G. Zamorani, M. Brusa, R. Gilli, K. Iwasawa, M. Salvato, F. Civano, M. Elvis, A. Merloni, A. Bongiorno, J. R. Trump, A. M. Koekemoer, E. Schinnerer, E. Le Floch, N. Cappelluti, K. Jahnke, M. Sargent, J. Silverman, V. Mainieri, F. Fiore, M. Bolzonella, O. Le Fèvre, B. Garilli, A. Iovino, J. P. Kneib, F. Lamareille, S. Lilly, M. Mignoli, M. Scodreggio, and D. Vergani, The x-ray to optical-uv luminosity ratio of x-ray selected type 1 agn in xmm-cosmos, *Astronomy and Astrophysics* **512**, A34 (2010).
- [108] F. Salvestrini, G. Risaliti, S. Bisogni, E. Lusso, and C. Vignali, Quasars as standard candles II: The non linear relation between UV and X-ray emission at high redshifts, *Astron. Astrophys.* **631**, A120 (2019), [arXiv:1909.12309 \[astro-ph.GA\]](#).
- [109] S. Bisogni, E. Lusso, F. Civano, E. Nardini, G. Risaliti, M. Elvis, and G. Fabbiano, The Chandra view of the relation between X-ray and UV emission in quasars, *Astron. Astrophys.* **655**, A109 (2021), [arXiv:2109.03252 \[astro-ph.GA\]](#).
- [110] O. Luongo, M. Muccino, E. Ó Colgáin, M. M. Sheikh-Jabbari, and L. Yin, Larger H0 values in the CMB dipole direction, *Phys. Rev. D* **105**, 103510 (2022), [arXiv:2108.13228 \[astro-ph.CO\]](#).
- [111] X. D. Jia, J. P. Hu, J. Yang, B. B. Zhang, and F. Y. Wang, Eiso–Ep correlation of gamma-ray bursts: calibration and cosmological applications, *Mon. Not. Roy. Astron. Soc.* **516**, 2575 (2022), [arXiv:2208.09272 \[astro-ph.HE\]](#).
- [112] N. Khadka, O. Luongo, M. Muccino, and B. Ratra, Do gamma-ray burst measurements provide a useful test of cos-

- mological models?, *JCAP* **09**, 042, [arXiv:2105.12692 \[astro-ph.CO\]](#).
- [113] L. Amati *et al.*, Intrinsic spectra and energetics of BeppoSAX gamma-ray bursts with known redshifts, *Astron. Astrophys.* **390**, 81 (2002), [arXiv:astro-ph/0205230](#).
- [114] H. Velten and S. Gomes, Is the Hubble diagram of quasars in tension with concordance cosmology?, *Phys. Rev. D* **101**, 043502 (2020), [arXiv:1911.11848 \[astro-ph.CO\]](#).
- [115] E. B. Holm, L. Herold, T. Simon, E. G. M. Ferreira, S. Hannestad, V. Poulin, and T. Tram, Bayesian and frequentist investigation of prior effects in EFT of LSS analyses of full-shape BOSS and eBOSS data, *Phys. Rev. D* **108**, 123514 (2023), [arXiv:2309.04468 \[astro-ph.CO\]](#).
- [116] E. B. Holm, A. Nygaard, J. Dakin, S. Hannestad, and T. Tram, Prospect: A profile likelihood code for frequentist cosmological parameter inference (2023), [arXiv:2312.02972 \[astro-ph.CO\]](#).
- [117] M. Demianski, E. Piedipalumbo, D. Sawant, and L. Amati, Cosmology with gamma-ray bursts: I. The Hubble diagram through the calibrated $E_{p,i} - E_{iso}$ correlation, *Astron. Astrophys.* **598**, A112 (2017), [arXiv:1610.00854 \[astro-ph.CO\]](#).
- [118] M. Demianski, E. Piedipalumbo, D. Sawant, and L. Amati, Cosmology with gamma-ray bursts: II Cosmography challenges and cosmological scenarios for the accelerated Universe, *Astron. Astrophys.* **598**, A113 (2017), [arXiv:1609.09631 \[astro-ph.CO\]](#).
- [119] O. Luongo and M. Muccino, Model-independent calibrations of gamma-ray bursts using machine learning, *Mon. Not. Roy. Astron. Soc.* **503**, 4581 (2021), [arXiv:2011.13590 \[astro-ph.CO\]](#).
- [120] A. C. Alfano, S. Capozziello, O. Luongo, and M. Muccino, Cosmological transition epoch from gamma-ray burst correlations (2024), [arXiv:2402.18967 \[astro-ph.CO\]](#).
- [121] H. Wang and N. Liang, Cosmological constraints on long gamma-ray bursts from fermi observations (2024), [arXiv:2405.14357 \[astro-ph.CO\]](#).
- [122] D. Rubin, G. Aldering, M. Betoule, A. Fruchter, X. Huang, A. G. Kim, C. Lidman, E. Linder, S. Perlmutter, P. Ruiz-Lapuente, and N. Suzuki, Union through unity: Cosmology with 2,000 sne using a unified bayesian framework (2023), [arXiv:2311.12098 \[astro-ph.CO\]](#).
- [123] DES, T. M. C. Abbott, M. Acevedo, M. Aguena, A. Alarcon, S. Allam, O. Alves, A. Amon, F. Andrade-Oliveira, J. Annis, P. Armstrong, J. Asorey, S. Avila, D. Bacon, B. A. Bassett, K. Bechtol, P. H. Bernardinelli, G. M. Bernstein, E. Bertin, J. Blazek, S. Bocquet, D. Brooks, D. Brout, E. Buckley-Geer, D. L. Burke, H. Camacho, R. Camilleri, A. Campos, A. C. Rosell, D. Carollo, A. Carr, J. Carretero, F. J. Castander, R. Cawthon, C. Chang, R. Chen, A. Choi, C. Conselice, M. Costanzi, L. N. da Costa, M. Crocce, T. M. Davis, D. L. DePoy, S. Desai, H. T. Diehl, M. Dixon, S. Dodelson, P. Doel, C. Doux, A. Drlica-Wagner, J. Elvin-Poole, S. Everett, I. Ferrero, A. Ferté, B. Flaugher, R. J. Foley, P. Fosalba, D. Friedel, J. Frieman, C. Frohmaier, L. Galbany, J. García-Bellido, M. Gatti, E. Gaztanaga, G. Gianini, K. Glazebrook, O. Graur, D. Gruen, R. A. Gruendl, G. Gutierrez, W. G. Hartley, K. Herner, S. R. Hinton, D. L. Hollowood, K. Honscheid, D. Huterer, B. Jain, D. J. James, N. Jeffrey, L. Kelsey, S. Kent, R. Kessler, A. G. Kim, R. P. Kirshner, E. Kovacs, K. Kuehn, O. Lahav, J. Lee, S. Lee, G. F. Lewis, T. S. Li, C. Lidman, H. Lin, J. L. Marshall, P. Martini, J. Mena-Fernández, F. Menanteau, R. Miquel, J. J. Mohr, J. Mould, J. Muir, A. Möller, E. Neilsen, R. C. Nichol, P. Nugent, R. L. C. Ogando, A. Palmese, Y. C. Pan, M. Paterno, W. J. Percival, M. E. S. Pereira, A. Pieres, A. A. P. Malagón, B. Popovic, A. Porredon, J. Prat, H. Qu, M. Raveri, M. Rodríguez-Monroy, A. K. Romer, A. Roodman, B. Rose, M. Sako, E. Sanchez, D. S. Cid, M. Schubnell, D. Scolnic, I. Sevilla-Noarbe, P. Shah, J. A. Smith, M. Smith, M. Soares-Santos, E. Suchyta, M. Sullivan, N. Suntzeff, M. E. C. Swanson, B. O. Sánchez, G. Tarle, G. Taylor, D. Thomas, C. To, M. Toy, M. A. Troxel, B. E. Tucker, D. L. Tucker, S. A. Uddin, M. Vincenzi, A. R. Walker, N. Weaverdyck, R. H. Wechsler, J. Weller, W. Wester, P. Wiseman, M. Yamamoto, F. Yuan, B. Zhang, and Y. Zhang, The dark energy survey: Cosmology results with 1500 new high-redshift type ia supernovae using the full 5-year dataset (2024), [arXiv:2401.02929 \[astro-ph.CO\]](#).
- [124] D. Foreman-Mackey, D. W. Hogg, D. Lang, and J. Goodman, emcee: The MCMC Hammer, *Publ. Astron. Soc. Pac.* **125**, 306 (2013), [arXiv:1202.3665 \[astro-ph.IM\]](#).
- [125] A. Lewis, Getdist: a python package for analysing monte carlo samples (2019), [arXiv:1910.13970 \[astro-ph.IM\]](#).